Tina Georg

Links between climate and the upper ocean structure: the Canary current upwelling system case

UNIVERSIDADE DO ALGARVE

FACULDADE DE CIÊNCIAS E TECNOLOGIA

2020

Tina Georg

Links between climate and the upper ocean structure: the Canary current upwelling system case

Master in Marine and Coastal Systems

Mestrado em Sistemas Marinhos e Costeiros

Worked performed under the supervision of:

Maria C. Neves, Universidade do Algarve (Supervisor)

Paulo Relvas, CCMAR, Universidade do Algarve (Co-Supervisor)

UNIVERSIDADE DO ALGARVE

FACULDADE DE CIÊNCIAS E TECNOLOGIA

2020

Links between climate and the upper ocean structure: the Canary current upwelling system case

Declaração de autoria de trabalho

Declaro ser o(a) autor(a) deste trabalho, que é original e inédito. Autores e trabalhos consultados estão devidamente citados no texto e constam da listagem de referências incluída.

Declaration of authorship of work

I declare to be the author of this work, which is original and unpublished. Authors and works consulted are duly cited in the text and are included in the list of references.

Faro, September 30th, 2020

Copyright

Acknowledgments

First of all, I would like to thank my supervisors Maria Neves and Paulo Relvas for giving me the opportunity to write my thesis combining the expertise of both and for their support throughout the whole process. Despite the special times, they always took the time to respond to emails and meet virtually when I had questions. I am also very grateful for their encouragement and help presenting an early stage of my results at the EGU2020 online conference to gather some additional experience. Maria Neves' believe in my abilities to learn Python and her input was very helpful and made it possible for me to write the thesis as it is.

I am very gratful for my friends near and far for being there along the way. It means a lot to me to know you by my side in good and in harder times. A special thanks to the ones that supported me during the process of writing my thesis.

Finally, I would like to thank my family. I am forever grateful for your support and for always believing in me. This wouldn't have been possible without you.

Abstract

Upwelling in the Eastern Boundary Currents is wind-driven. Ekman transport off the coast of the Canary Current Upwelling System (CCUS) is induced by equatorward, alongshore trade winds leading to persistent upwelling of cooler subsurface water throughout the year. This study uses Upwelling Indices (UI) between 25 and 35°N to assess upwelling in the CCUS and relates it to the changes in the upper ocean structure as well as climate indices. Upwelling was determined using different approaches such as differences in the Sea Surface Temperature (SST) at the coast and offshore (UI_{SST}), and the prevailing wind conditions with the resulting Ekman transport (UI_{w}). Within the study area, the detection of upwelling varies on a temporal and spatial scale depending on the different determination methods of the UI's. These results imply that the existing indices need an adaptation to be more reliable. Nevertheless, all indices revealed strong upwelling events along a wider shelf between 25 and 33°N and some downwelling events along a narrow shelf between 33 and 35°N. A significant correlation was found between the UI's and the vertical structure of the upper ocean which is especially represented by the isothermal layer depth (ILD). In regards to the prevailing climate, the North Atlantic Oscillation (NAO) influences the location and strength of the westerly and trade winds in the study area. Its strong signal during winter (December to March) is reflected in significant correlations between the NAO and all parameters, however, when considering the correlations for the whole year, its signal is ambiguous. The NAO correlates well with the UI's and the ILD. During its positive phase, cooler temperatures can be observed at the coast indicating upwelling. Simultaneously, the ILD deepens at the coast and becomes shallower offshore which is reversed in NAO- years and enhanced during coupled, opposite phases with the East Atlantic pattern. Still, upwelling occurs in years of a neutral NAO so it cannot be ascribed as the main driver for upwelling processes in the area. The interplay of upwelling, vertical structure and climate is rather due to a complex system of different forcings and cause-effect relationships. Ocean dynamics related to the kinetic and potential energy as well as the thermohaline circulation in its long-term variability may have an impact on these variables on different temporal and spatial scales.

Key Words: Canary Current Upwelling System (CCUS), Upwelling Indices, Isothermal Depth Layer (ILD), North Atlantic Oscillation (NAO), Upper Ocean Structure

Resumo

O afloramento nas fronteiras leste dos oceanos é induzido pelo vento. O transporte de Ekman ao largo da costa do Canary Current Upwelling System (CCUS) é induzido por ventos alísios ao longo da costa, em direção ao equador, que levam ao afloramento persistente de águas subsuperfícies mais frias ao longo do ano. Este estudo usa índices do afloramento (UI) entre 25 e 35°N para avaliar o afloramento no CCUS e relaciona-o com as mudanças na estrutura das camadas superiores do oceano, bem como os índices climáticos. O afloramento foi inferido usando diferentes abordagens, como as diferenças na temperatura da superfície do mar (SST, UI_{SST}), as condições de vento prevalecentes e o transporte de Ekman resultante (UI_w). Na área de estudo, a deteção do afloramento varia com a escala temporal e espacial dependendo dos diferentes métodos de determinação dos UI. Esses resultados implicam que os índices existentes necessitam de uma adaptação para serem mais confiáveis. No entanto, todos os índices revelaram fortes eventos do afloramento ao longo de uma plataforma mais ampla entre 25 e 33°N e alguns eventos do afloramento ao longo de uma plataforma estreita entre 33 e 35°N. Foi encontrada uma correlação significativa entre a UI e a estrutura vertical da camada superior do oceano que é especialmente representada pela profundidade da camada isotérmica (ILD). Em relação ao clima predominante, a Oscilação do Atlântico Norte (NAO) influência a localização e intensidade dos ventos de oeste e alísios na área de estudo. A sua maior intensidade no inverno (dezembro a março) se reflete em correlações significativas entre o NAO e a IU e a ILD. Durante a sua fase positiva, temperaturas podem ser observadas mais baixas na costa indicando afloramento. Simultaneamente, a ILD torna-se mais profunda ao longo da costa e mais superficial ao largo, o que é revertido em anos NAO- e mais intensificado durante as fases opostas acopladas ao padrão do Atlântico Leste. A correlação entre o NAO e as UI's e a ILD não é clara quando olha-se para o ano todo e o afloramento ocorre mesmo em anos de NAO neutra, portanto NAO não pode ser considerado a principal causa dos processos de afloramento na área. A interação entre o afloramento, a estrutura vertical do oceano e o clima é mais devida a um sistema complexo de diferentes forças e relações de causa-efeito, como a dinâmica do oceano em relação à energia cinética e potencial, bem como a circulação termohalina e sua variabilidade de longo prazo em diferentes períodos de tempo e escalas espaciais.

Resumo alargado

Resumo alargado O afloramento ao longo das fronteiras leste dos oceanos tem sido objeto muitos estudos oceanográficos e biológicos. Os ventos na direção do Equador ao atuar na superfície do oceano induzem um transporte de Ekman para o largo, causando o movimento vertical de águas subsuperficiais mais frias em direção à superfície. Como a água é rica em nutrientes, o aumento da produtividade biológica é evidente. Mudanças nas propriedades oceanográficas da estrutura das camadas superiores do oceano são objeto de investigação.

Este estudo foca-se no regime de afloramento no Oceano Atlântico Norte entre 25 e 35°N, que faz parte do Sistema de Afloramento da Corrente das Canárias (CCUS). Os principais objetivos são a deteção de eventos de afloramento, a avaliação da estrutura do oceano superior e suas mudanças com o afloramento, e o papel do padrão climático, assim como da Oscilação do Atlântico Norte (NAO) no afloramento e na estrutura do oceano superior. O período do estudo foi de 25 anos (1993-2017).

Existem várias abordagens diferentes para inferir o afloramento costeiro no oceano. O índice de afloramento (UI) mais comum é baseado na diferença térmica da água de superfície na costa e no mar ao largo. A avaliação pode ser feita facilmente usando imagens de satélite e ferramentas de deteção remota. No estudo atual, o índice foi calculado usando a temperatura da superfície ($_{SST}$) do Global Ocean Ensemble Physics Reanalysis (GREP) fornecido pelo Copernicus Monitoring Environment Marine Service (CMEMS). Outro método é o uso de dados de vento. A direção do vento em conjunto com a tensão do vento permite calcular a direção e intensidade do transporte Ekman e assim inferir o afloramento levando em consideração a geometria da linha da costa. Para calcular o IU com base no vento (UI_w), foi usada a quinta versão global da Re-análise ECMWF (ERA5) obtida do Centro Europeu de Previsões Meteorológicas de Médio Prazo (ECMWF), bem como dados do Pacific Fisheries Environmental Laboratory (PFEL) da National Oceanic and Atmospheric Administration (NOAA). Todos os índices foram calculados e comparados. O resultado concorda com as descobertas anteriores de que a área de estudo selecionada entre 25 e 35°N é caracterizada por afloramento anual permanente com eventos fortes durante o verão e outono. Ainda assim, a distribuição temporal e espacial dos eventos varia com o índice selecionado e torna-se evidente um intervalo até 5 meses entre a IU baseada no vento e

aquela baseada na Temperatura da Superfície do Mar (SST). Este facto sugere a necessidade de um índice adequado que entre em linha de conta com a dinâmica prevalecente.

Os resultados também revelam uma mudança na intensidade do afloramento em 32.5°N, que acompanha uma mudança na plataforma continental de larga para estreita e com mudanças no vento. Usando uma regressão linear, foram calculadas as tendências de todas os IUs a fim de comparar os valores encontrados com os resultados controversos existentes sobre a alteração do número e intensidade dos eventos relacionados com a mudança climática. Novamente os resultados variam com o índice usado. No entanto, nenhuma tendência clara foi detetada nos últimos 25 anos em qualquer um deles.

Para a análise da estrutura da camada superior do oceano, foi determinada a profundidade da camada isotérmica (ILD), que é a profundidade máxima da interação oceano-atmosfera com propriedades da água quase homogêneas. Para todo o conjunto de dados do GREP, foi encontrada a profundidade na qual a temperatura é 0.8°C mais fria do que a temperatura de referência a 10 m abaixo da superfície. O ILD é profundo no inverno e superficial durante os meses de verão, o que é consequência da variabilidade temporal na energia cinética e potencial trocadas nas camadas superiores do oceano. O ILD mais profundo foi encontrado em março a 199,79 m próximo da costa, e 244,89 m em mar aberto, e o mais raso ocorre entre julho e outubro e é igual ao nível de referência. A fim de avaliar a estrutura vertical do oceano durante os eventos de afloramento e afundamento (upwelling/downwelling), forma construídas secções compostas baseadas no conjunto da temperatura potencial dos dados GREP nas duas situações. Os resultados mostram um gradiente ascendente das isotérmicas para a costa nos eventos de afloramento que representa o movimento vertical da água mais fria para a superfície. Durante os eventos de afundamento (downwelling), as isotérmicas decaem da costa para o largo, embora com menor declive e são mais paralelas entre si. Estes resultados estão em concordância com o mecanismo de Ekman (Ekman pumping). Além disso mostram uma camada superficial mais profunda com temperaturas constantes durante os eventos de downwelling identificados no IU com base nos dados ERA5 (UI_{ERA5}). Em geral, descobriu-se que o ILD é mais profundo durante o afloramento e torna-se mais superficial durante os eventos de *downwelling* (afundamento).

Ao correlacionar os resultados anteriores com a NAO, verifica-se uma correlação alta e sig-

nificativa com o UI_{ERA5}. O mesmo se aplica para o UI_{SST}, embora a correlação seja menor. Considerando o ILD, um afundamento do ILD próximo da costa pode ser observado durante os meses de inverno de anos NAO positivos, bem como durante as fases acopladas a um valor negativo do padrão do Atlântico Leste (EA). O sinal é invertido durante os anos de NAO- e NAO-EA+. Essas correlações e mudanças podem ser atribuídas a mudanças no padrão de vento sobrejacente.

Como a NAO e o padrão EA estão relacionados com a Alta Pressão dos Açores, as mudanças nos ventos de oeste e nos ventos alísios são o resultado da fase correspondente do padrão. Os diferentes padrões de vento e o impacto máximo na profundidade foram representados em mapas compostos horizontais. Embora exista uma relação entre o clima e os índices de afloramento, bem como com a estrutura do oceano superior, não é possível considerar a NAO como o principal fator forçador para ambos. O afloramento não ocorre em todos os anos com a NAO positiva e também ocorre em anos em que a NAO é neutro. O mesmo se aplica à ILD que tem seu ciclo anual bem definido, mas que é modulado pela fase da NAO e as suas fases acopladas com o EA. Em geral, o ILD é mais profundo perto da costa e mais superficial ao largo durante os meses de inverno dos anos NAO+ e NAO+EA- e o oposto ocorre durante os anos NAO- e NAO-EA+. Ainda assim, outros fatores como o forçamento da SST pelo o fluxo de calor do oceano e pela circulação termohalina, com feedbacks em diferentes escalas de tempo, precisam ser considerados para obtermos boas previsões para eventos futuros.

Palavras-chave: Sistema de afloramento da corrente das Canárias, Índices de afloramento, Profundidade da camada isotérmica, Oscilação do Atlântico Norte (NAO), Estrutura do oceano superior.

Contents

List of Figures

List of Tables

List of Abbreviations

AMO	Atlantic Multidecadal Oscillation
AMOC	Atlantic Meridional Overturning Circulation
CCUS	Canary Current Upwelling System
C-GLORS	CMCC Global Ocean Reanalysis System
CMCC	Centro Euro-Mediteraneo sui Cambiamenti Climatici (Euro-Mediterranean Center for Climate Change)
CMEMS	Copernicus Monitoring Environment Marine Service
EA	East Atlantic pattern
EBC	Eastern Boundary Current
ECMWF	European Centre for Medium-Range Weather Forecasts
ENSO	El Niño-Southern Oscillation
ERA5	ECMWF Re-Analysis, fifth global version
ERDDAP	Environmental Research Division Data Access Protocol server
FOAM	Forecast Ocean Assimilation Model
FTP	File Transfer Protocol
GLORYS	Global Ocean Reanalysis and Simulation
GLOSEA	Global Seasonal forecast system
GREP	Global Ocean Ensemble Physics Reanalysis
GSW	Gibbs Seawater
ILD/MLD	Isothermal/Mixed Layer Depth
IPCC	Intergovernmental Panel on Climate Change
NAO	North Atlantic Oscillation
NEMO	Nucleus for European Modelling of the Ocean
NOAA	National Oceanic and Atmospheric Administration
ORAS5	Ocean Re-Analysis System-5
ORCA025	Generic name of global ocean configurations (uses horizontal curvilinear mesh, 1/4° grid resolution)
PDO	Pacific Decadal Oscillation

PFEL	Pacific Fisheries Environmental Laboratory
PSU	Practical Salinity Unit
QGIS	Quantum Geographic Information System
SCAND	Scandinavian pattern
SLP	Sea Level Pressure
SST	Sea Surface Temperature
TEOS-10	Thermodynamic Equation of Seawater - 2010
UI	Upwelling Index
WOA18	World Ocean Atlas Version 2018

1 Introduction

The upwelling regime of the Eastern Boundary Currents has a great impact on the primary production of the ocean's ecosystem (i.e. Arístegui et al. 2009, Carr and Kearns 2003, Gruber et al. 2011, Messié and Chavez 2015, Santos et al. 2005, Troupin et al. 2010). As the Canary Current upwelling system along with the California Current, the Humboldt Current and the Benguela Current cover about one percent of the ocean but make up for five percent of the primary production and more than 20 percent of the fish catch, the economic and scientific importance of these systems is evident (Bonino et al. 2019, Carr and Kearns 2003, Chavez and Messié 2009, Cropper et al. 2014).

With cooler subsurface water being brought to the surface, upwelling in the ocean becomes visible in the differences of Sea Surface Temperatures (SST) between the coast and the offshore area as a result of an increased Ekman transport off the coast. The latter is caused by alongshore wind flowing towards the equator (i.e. Bakun 1990, Bakun and Nelson 1991, Barton et al. 2013, Benazzouz et al. 2014, Cropper et al. 2014, Ramos et al. 2013). While these factors describe the processes on the sea surface, variations in the intensity of the regime can also be seen in the vertical structure of the ocean since the extension of the mixed layer and the location of the thermocline varies with Ekman suction and pumping related to up- and downwelling processes (Bonino et al. 2019, Visbeck et al. 2003). Past studies mainly focused on the surface of the ocean to determine upwelling and to characterize its intensity (i.e. Polonsky and Serebrennikov 2018, Ramos et al. 2013). Barton et al. (1998) considered the vertical structure in their study using the depth of the thermocline and biological productivity mainly for the investigation of upwelling filaments. Other studies focus on the mixed layer and possible forcings on its depth in the global ocean (Bonino et al. 2019, Delworth and Zeng 2016, Delworth et al. 2017, Rodwell et al. 1999). For the Canary Current, Bessa et al. (2017, 2018, 2019, and 2020) studied the mixed layer depth in correlation with upwelling and climate pattern, however, the main cause-effect relationship is yet to be established. This study aims to analyze the vertical structure and its correlation pattern with possible drivers.

One of the main focuses will be the correlation of upwelling and the vertical structure with climate patterns such as the North Atlantic Oscillation (NAO) and its coupled phases with the

East Atlantic pattern (EA) to assess the role of climate on the upwelling structure. Both patterns have been identified as a major driver for the climate and sea level anomalies in Europe and north Africa (Barnston and Livezey 1987, Bastos et al. 2016, Hurrell et al. 2001, Trigo et al. 2004, Knippertz et al. 2003, Yan et al. 2004). Correlations between the NAO in particular and the upwelling intensity of the Canary Current have been found in several studies in the past (i.e. Benazzouz et al. 2014, Cropper et al. 2014, McGregor et al. 2007, Narayan et al. 2010, Santos et al. 2005). In addition to these researches, this study aims to investigate the relationship between climate and the vertical structure of the ocean in the central part of the Canary Current Upwelling System (CCUS). The study area is defined between 25 and 35°N where upwelling occurs throughout the year with an intensification between June and September (Wooster et al. 1976). The time span of the study was set to 25 years (1993-2017).

In summary, three main objectives have been defined to investigate upwelling and the vertical structure of the ocean. Firstly, upwelling will be identified using conventional indices defined in past studies. Therefore, SST and wind data will be used to calculate upwelling indices.

For the second objective, the three-dimensional structure of the ocean will be assessed using vertical composite maps and profiles. Using in-situ and modeled data from international organizations, the vertical structure will be extracted on different spatial and temporal scales. Additionally, the depth of the mixed layer will be determined on a seasonal and annual scale in order to gather information about the interannual variability.

In a third step, the results from the first and the second objectives will be correlated with prevailing climate indices, namely the NAO and its coupled phase with the EA. The selected study area with different intensities of upwelling throughout the year is expected to give a good insight into the changes of all factors with the annual variations and, therefore, allows to establish possible relationships.

2 State of the Art

Upwelling is a major field of research in physical oceanography and marine biology as it is a unique feature in the ocean with a range of different processes acting together (Hughes and Barton 1974). It occurs within the Eastern Boundary Currents and leads to changes in the upper ocean structure. In the following section, the main areas of upwelling, the stratification of the ocean, and the different approaches of its detection will be presented along with the prevailing climate pattern of the Atlantic Ocean.

2.1 Eastern Boundary Currents

The world's ocean feature four Eastern Boundary Currents (EBC) which are highly productive regions (Barton et al. 2013, Ryther 1969). As the name implies, these currents expand along the coast of the eastern part of ocean basins with a north to south elongation. In the Pacific Ocean, there is the California Current in North America and the Humboldt/Peru-Chile Current along the South American shelf. In the Atlantic, the Canary Current flows along the Iberian Shelf and the Moroccan coast in the north and the Benguela/Lüderitz Current in the south of Africa (Carr and Kearns 2003, Chavez and Messié 2009, Messié and Chavez 2015).

All EBCs are defined by upwelling processes driven by prevailing wind conditions as well as local and remote forcings such as stratification. For the Pacific Ocean, the El Niño-Southern Oscillation (ENSO) modulates winds and, therefore, upwelling in both systems. In the Atlantic Ocean, different climate modes are the driver for the wind in the Canary Current Upwelling System (CCUS, see chapter 2.2) and a positive trend in upwelling is forced by sea level pressure trends in the Benguela Current. The systems in both oceans are independent from each other (Bonino et al. 2019).

In regards to climate change, a controversy exists in the scientific community about its effects on upwelling processes. Bakun (1990) uses the correlation of the wind stress and upwelling intensity as a measure to determine an intensification of upwelling with an increase in the CO_2 and further greenhouse gas concentrations in the atmosphere. His hypothesis is based on an increased on- to offshore pressure gradient and, therefore, increasing alongshore winds and up-

welling. The same trends are shown by McGregor et al. (2007) detecting a cooling trend in the SST around Cape Ghir, by Polonsky and Serebrennikov (2018) showing an increase in the trade winds and by Narayan et al. (2010) considering different wind data, however, the latter study reveals conflicting results based on the data set. Cropper et al. (2014) suggest a modification of Bakun's hypothesis for the summer month in the northwest of Africa at 20°N according to the differences in the influence of the north-eastern trade winds above and the south-western monsoon below that latitude.

Contrary to these studies, Bonino et al. (2019) and Pardo et al. (2011) found a decrease in the upwelling intensity for the Canary Current and sections of other EBCs (Humboldt and Benguela Current) with a strong seasonal difference. Barton et al. (2013) detected an increase in the SST of >0.01°C per year along the Canary Current and no significant changes in the meridional winds, hence, no intensification in upwelling. These findings are confirmed by studies about the net primary production (Gómez-Letona et al. 2017).

The contradictory results show the importance of research in this area. As Sydeman et al. (2014) and the Intergovernmental Panel on Climate Change (IPCC 2019) found weakening of wind intensity for the Canary Current and an intensification for the other EBCs it is also important to look at all systems and their prevailing drivers separately in order to make more precise predictions about future changes.

2.2 The Canary Current Upwelling System

The Canary Current, a southward flowing current on the surface of the north-western Atlantic with a poleward undercurrent, expands from the Iberian Peninsula at 43°N along the north-western coast of Africa to the the south of Senegal (8°N, Knoll et al. 2002). Due to the variability in the upwelling regimes related to the annual shift of the north-eastern trade winds and intraannual changes of the Azores High, the system can be divided into three sections (fig. 2.1). In the Mauretania-Senegalese Upwelling Zone south of 20°N and the Portuguese and Galician Upwelling Zone along the Iberian Shelf north of 35°N, upwelling occurs predominantly during the winter or summer month, respectively (Barton et al. 2013). Nykjær and Van Camp (1994) found that the interannual variability of the seasonal upwelling is greatest in the Mauretania-Senegalese

Upwelling Zone as the influence of the trade winds is replaced by the monsoon winds in summer and autumn. In the center of the system, upwelling can be observed permanently with an intensification during fall and spring (i.e. Santos et al. 2005). Cropper et al. (2014) and Nykjær and Van Camp (1994) also divide the central area at 25 or 26°N, respectively, into strong (south) and weak (north) permanent annual upwelling in dependency of the annual migration of the trade winds.

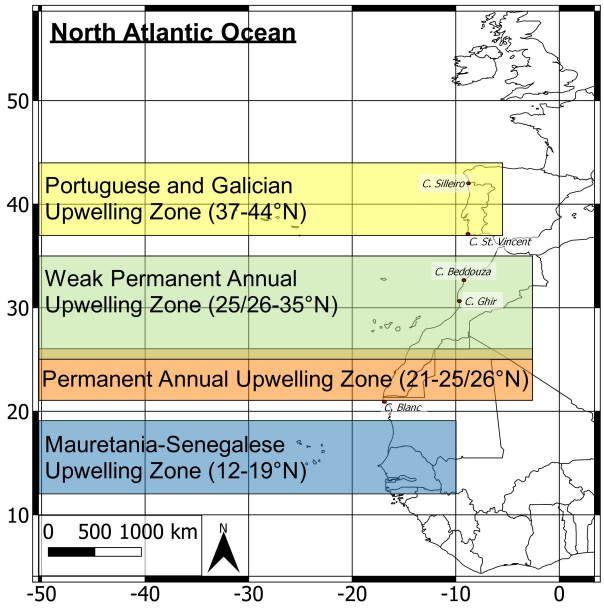

Figure 2.1: The Canary Current upwelling regions. Schematic map of northwestern Africa and the Iberian Peninsula showing the areas of different upwelling regimes (map created in QGIS, modified after: Arístegui et al. 2009, Cropper et al. 2014 and Nykjær and Van Camp 1994).

This study will focus on the area between 25 and 35°N which is representing the central part of the Canary Current upwelling system and, therefore, persistent upwelling throughout the year with an annual cycle and strongest events from June to September (Bessa et al. 2018, Wooster et al. 1976). These characteristics are expected to allow the establishment of relationships between upwelling, the vertical structure and the climate patterns as the annual variability and changes in the intensities of upwelling in summer makes it easier to identify possible drivers. The study area includes Cap Ghir at the Moroccan coast and the Canary Islands. The continental shelf is wide up to 33°N and narrow above. Even though the overall orientation of the coastline is from south-west to north-east, the study area comprises different angles of the coastline which can influence the upwelling intensity (fig. 2.2, see also section 2.4). There is no freshwater input

in the selected area (Arístegui et al. 2009). As the study area combines different features, it is expected that different impacts on the processes can be assessed.

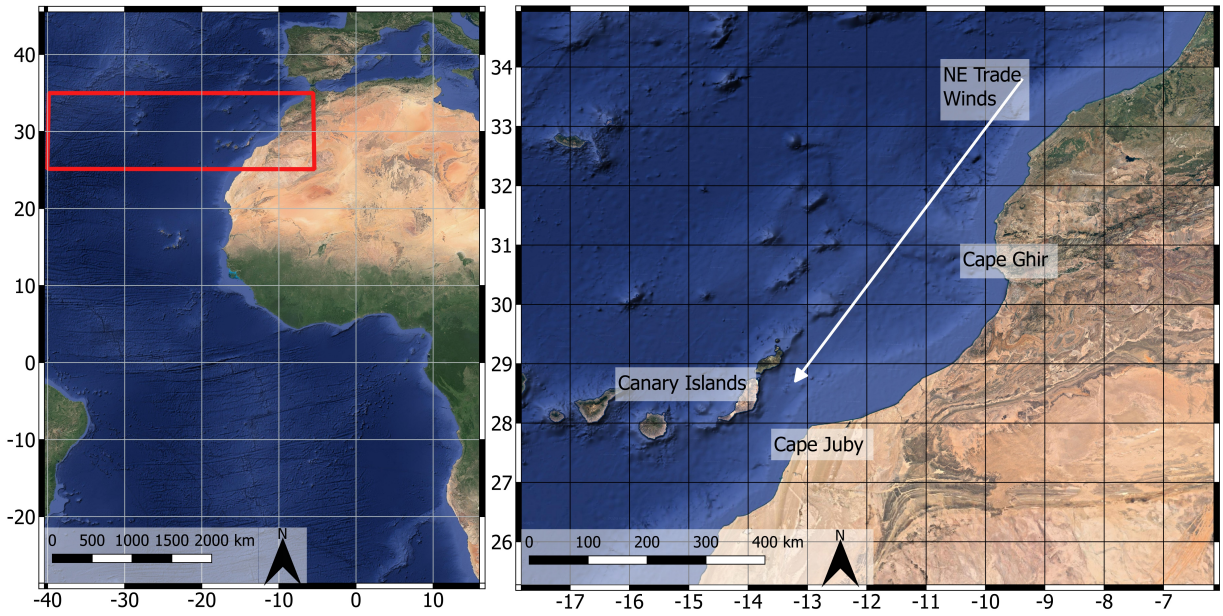

(a) Location in the Atlantic Ocean **(b)** Coastal area of the study site

Figure 2.2: Map of the study site. The location in the Atlantic Ocean (a) and the study area showing the coastline orientation and the mean direction of the trade winds (b, maps created in QGIS).

2.3 Ocean Stratification

The stratification of the ocean is closely related to the temperature and density (Hughes and Barton 1974). On the surface and the upper layer, changes in the kinetic energy from winds, storms, waves, or horizontal advection by currents, and in the potential energy resulting from freshwater inputs impact the turbulence in the upper ocean and lead to mixing of the water up to a certain depth (Balaguru et al. 2016, Hu et al. 2019, Mawren and Reason 2017, Sprintall and Tomczak 1992). In this surface mixed (density) and isothermal layer (temperature), the physical properties are 'quasi-homogeneous' with a small variation and the depths representing the extent of the ocean-atmosphere interaction (Chu and Fan 2011, Sprintall and Tomczak 1992). Additionally, the solar radiation, sensible and latent heat fluxes at the surface along with the prevailing wind influence the heat content (Wm^{-2}) in the isothermal layer (Gnanaseelan et al. 2003, Yu and Weller 2007). A deeper isothermal layer increases the heat capacity of the ocean and

its sensitivity to surface cooling which makes the depth of the layer a good indicator for ocean warming in the past decades (Levitus et al. 2000, Yamamoto et al. 2020, Willis 2004). Still, ocean warming does not imply an increase in the stratification and it is important to consider the isothermal layer depth (ILD) independent from the surface (SST) warming as the former is dependent on the scale of the sea-air-interaction and additional forcings (Polonsky 1995, Somavilla et al. 2017). Bessa et al. (2018) found a negative correlation between the mixed layer depth (MLD) and the SST along the Moroccan coast which was also observed in other regions of the ocean (Whitney and Freeland 1999). In terms of biological productivity, a deeper mixed layer enhances ocean ventilation and the vertical supply of nutrients (Yamaguchi and Suga 2019) but the highest productivity and algae blooms occur when the mixed layer depth is getting shallower in spring (Obata et al. 1996, Sverdrup 1953). Below the mixed layer, the deep ocean starts with a strong thermo-, halo- and pycnocline indicating a high level of stratification with stable conditions (Bessa et al. 2020).

In the transition of surface and deep ocean water, a gap can exist between the bottom of the mixed layer and the top of the thermocline. This gap is defined as barrier layer and is mainly related to the kinetic and potential energy (Kara et al. 2000, Lukas and Lindstrom 1991, Pailler et al. 1999, Sprintall and Tomczak 1992, Tanguy et al. 2010). The barrier layer varies with seasons and the ocean area where it is found especially in the tropical oceans. For the North Atlantic Ocean, de Boyer Montégut et al. (2007) found a small barrier layer thickness (0-10 meter).

In terms of ocean stratification, Troupin et al. (2010) found a shallow MLD of around 20 m followed by a strong gradient of the thermo-, halo-, and pycnocline in the Canary Current south of Gran Canaria in late summer to early fall. This high stratification coincidies with the weakening of the trade winds in the region. The deepest ILD can be observed at around 100-150 m in February with a maximum heat release from the ocean into the atmosphere. Similar results have been found for other ocean areas while the mixed layer deepens from the equator to the pole (Bessa et al. 2018, Somavilla et al. 2017, Whitney and Freeland 1999).

The calculation of the ILD can be done using different approaches whereas the difference and gradient criterion are the easiest ones to use (Chu and Fan 2010, Chu and Fan 2011). The difference criterion uses the temperature (density) at a reference depth of 10 m and defines the ILD

(MLD) as the depth where the temperature (density) is by a fixed value smaller than the reference level temperature (density). Commonly, 0.5 to 0.8°C is used as the difference between the reference and the ILD (Kara et al. 2000, 0.03kg m^{-3} for the MLD). For the gradient criterion, the variation of temperature (density) with depth (δT/δz, $\delta\rho/\delta$z) is used to extract the depth where the variation exceeds a fixed value (i.e. 0.025°C m^{-1}, Lukas and Lindstrom 1991).
Besides providing an insight in the upper ocean structure, studies have suggested that there is a relationship between the ILD and upwelling activity (Nykjær and Van Camp 1994, Bessa et al. 2018). In models, Bonino et al. (2019) found the impact of local forcings such as the thermocline and the stratification as one driver of upwelling in the Canary Current along with the wind and remote forcings like coastal trapped waves. Therefore, the ocean stratification is an important aspect when studying upwelling and will be included in this study.

2.4 Upwelling Indices

Upwelling occurs when the water of the upper layer in the ocean is moved offshore due to Ekman transport which is induced by wind stress, friction, and the rotation of the Earth (Coriolis force). At the coast, these water masses are replaced by colder subsurface waters in a vertical motion (Ekman suction, Barton et al. 2013). In order to assess the upwelling and its intensity, upwelling indices are calculated using thermal differences as well as the wind stress of the equatorward alongshore winds resulting from changes in the north-eastern trade winds.
Using SST data, the coastal Upwelling Index (UI) is calculated based on the SST differences between the near- and the offshore temperature using the following equation (i.e. Benazzouz et al. 2014, Cropper et al. 2014, Fiúza et al. 1982, McGregor et al. 2007, Pelegrí and Benazzouz 2015, Polonsky and Serebrennikov 2018, Santos et al. 2011, Tamim et al. 2019):

$$UI_{SST(lat,time)} = SST_{offshore(lat,time)} - SST_{nearshore(lat,time)} \tag{1}$$

The SST differences are calculated cross-shore using in-situ measurements or satellite images. Positive index values indicate cooler water at the coast and relatively warmer water offshore and, therefore, upwelling. Even though the equation 1 is used by several authors, the definition

of both variables, $SST_{inshore}$ and $SST_{offshore}$, varies. Benazzouz et al. (2014) consider the local bathymetry of the shelf when determining the nearshore temperature ($SST_{inshore}$). In case of a narrow continental shelf, this reference point is close to the coast whereas it moves slightly offshore with a wider shelf. Other studies define the nearshore SST as ranges from the coast: Santos et al. (2005) used 20 to 40 km in their study, Ramos et al. (2013) 0 to 50 km. The same discrepancy becomes apparent with $SST_{offshore}$. As it depends on the region, the $SST_{inshore}$ and the upwelling intensity, authors suggest the usage of the SST between 400 km up to 3,000 km offshore (Benazzouz et al. 2014, Santos et al. 2005), however, 500 km is widely used in recent studies (i.e. Cropper et al. 2014, Marcello et al. 2011, Narayan et al. 2010, Ramos et al. 2013).

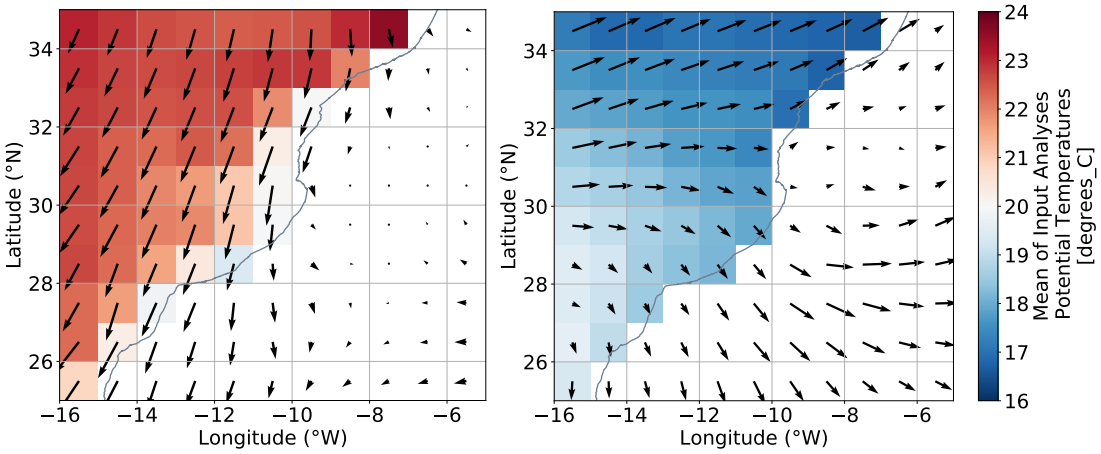

(a) Upwelling favorable wind conditions

(b) Downwelling favorable wind conditions

Figure 2.3: Up- and downwelling favorable wind conditions in the study area. Plot of the alongshore winds towards the equator favoring upwelling (a, September 1994) and towards the poles favoring downwelling (higher latitudes in b, December 2001) with the underying SST values (mean potential temperature). Wind speed represented by the size of each arrow (plot created in Python, wind data derived from ERA5, ECMWF Copernicus 2019, SST data: GREP, E.U. Copernicus Marine Service Information 2020).

In order to obtain a better understanding of the upwelling regime and its intensity, the wind stress can be used as main driver for coastal upwelling along the Eastern Boundary Currents. Wind stress of equatorward winds blowing parallel to the coast lead to an offshore Ekman transport (90°) of the surface layer, upwelling of cooler subsurface water to the surface and a lowering of the thermocline. Opposite conditions lead to the advection of water towards the coast and downwelling (Bakun 1973 and 1990, Freudenthal et al. 2002, Pelegrí and Benazzouz 2015, Wright

et al. 2001, fig. 2.3). In the CCUS, the north-eastern trade winds with an annual shift in their location as well as the position and strength of the Azores High play a major role in the variation of the wind stress (Barton et al. 1998, Benazzouz et al. 2014, Narayan et al. 2010, Polonsky and Serebrennikov 2018).

The calculation of the UI based on the wind data (UI_w) is done in three steps. Firstly, the zonal (τ_x) and meridional (τ_y) wind stress is computed using the wind speed (two components: W_x and W_y, equivalent to $\vec{u}$ and $\vec{v}$), the drag coefficient ($C_d = 1.14x10^{-3}$, dimensionless, Large and Pond 1981) and the density of the air ($\rho_a = 1.22\text{kg m}^{-3}$):

$$\tau_x = \rho_a C_d (W_x^2 + W_y^2)^{1/2} W_x \text{ and } \tau_y = \rho_a C_d (W_x^2 + W_y^2)^{1/2} W_\text{y} \tag{2}$$

In the second step, both wind stress variables are used in addition to the density of the sea water ($\rho_w = 1,025\text{kg m}^{-3}$) and the Coriolis parameter ($f = 2\Omega sin(\theta)$ with $\Omega = 7.292x10^{-5}s^{-1}$ and θ = latitude) to calculate the Ekman transport parallel and normal to the coastline (Q_x and Q_y, equation: 3). Thirdly, the UI_w can be computed considering the geometry of the adjacent coastline (φ = mean angle between shoreline and equator) and the Ekman transport (i.e. Bakun and Nelson 1991, Cropper et al. 2014, McGregor et al. 2007, Miller and Shanks 2004, Ramos et al. 2013, equation: 4).

$$Q_x = \frac{\tau_y}{\rho_w f} \text{ and } Q_y = \frac{-\tau_x}{\rho_w f} \tag{3}$$

$$UI_W = -sin(\varphi - \pi/2)Q_x + cos(\varphi - \pi/2)Q_y \tag{4}$$

This more complex calculation is expected to give more accurate results and characterization for specific regions as it considers local parameter of the coastline, the wind speed and direction. In comparison to the UI_{SST}, several studies have found a time lag of 0-2 month between both indices which can be due to several causes such as local topography, inertia differences of the atmosphere and the ocean, and advection processes (Benazzouz et al. 2014, Cropper et al. 2014, Fiúza et al. 1982, Nykjær and Van Camp 1994). For a better calculation of the UI's, Bessa et al. (2019) additionally suggest an implementation of the mixed layer depth (see ch. 2.3), however, there is no clear hypothesis on how to include the depth into an equation yet.

2.5 Climate Indices

Several climate patterns are known to impact the north Atlantic region in different aspects such as sea level and precipitation with related flooding and drought events (i.e. Bastos et al. 2016, Comas-Bru and Hernández 2018, Knippertz et al. 2003, Neves et al. 2019, Yan et al. 2004).
Due to their location and recent studies on their influence on Europe, climate patterns with possible influence in the study area are the Scandinavian pattern (SCAND), the Atlantic Multidecadal Oscillation (AMO), the NAO and the EA. The greatest impacts of the SCAND coincide with its geographic location over Scandinavia (Bueh and Nakamura 2007, Moore et al. 2013) and will, therefore, not be further considered in this study. The same applies for the AMO: Even though, Bonino et al. (2019) identified the AMO as main driver for the negative trend in the upwelling of the CCUS, its low-frequency mode of around 30-70 years makes it incompatible for the time span of the current study (Schlesinger and Ramankutty 1994, Wang et al. 2017, Yamamoto et al. 2020).
Since the influence of the NAO on the upwelling regime and ocean dynamics has been investigated by several studies with mostly significant correlations, it will also be used for the analysis in this study (i.e. Benazzouz et al. 2014, Bonino et al. 2019, McGregor et al. 2007, Narayan et al. 2010). The NAO is defined by the differences in the normalized sea level pressure (SLP) between Iceland (low pressure system) and the subtropical high in the Azores and has biennial to decadal frequency of occurrence (Hurrell et al. 2001, Hurrell et al. 2003). During years of a positive NAO (NAO+), the Icelandic Low pressure system is anomalously lower and the Azores High well defined leading to enhanced westerly winds, winds in the trade wind belt, and storms whereas in its negative state (NAO-) both pressure systems are weak causing a deceleration and southerly shift of the westerlies (Angell and Korshover 1974, Luo et al. 2007, Visbeck et al. 2003, phases of the climate pattern: fig. 2.4). Delworth and Zeng (2016) found a strengthening of the Atlantic Meridional Overturning Circulation (AMOC) in NAO+ phases along with anomalous heat fluxes. For the ocean's mixed layer depth in the North Atlantic Ocean, a model by Yamamoto et al. (2020) found a deepening in years of positive NAO as a result of anomalies in the wind stress.
Similar effects result from the EA, however, the dipole is shifted towards the southeast with a

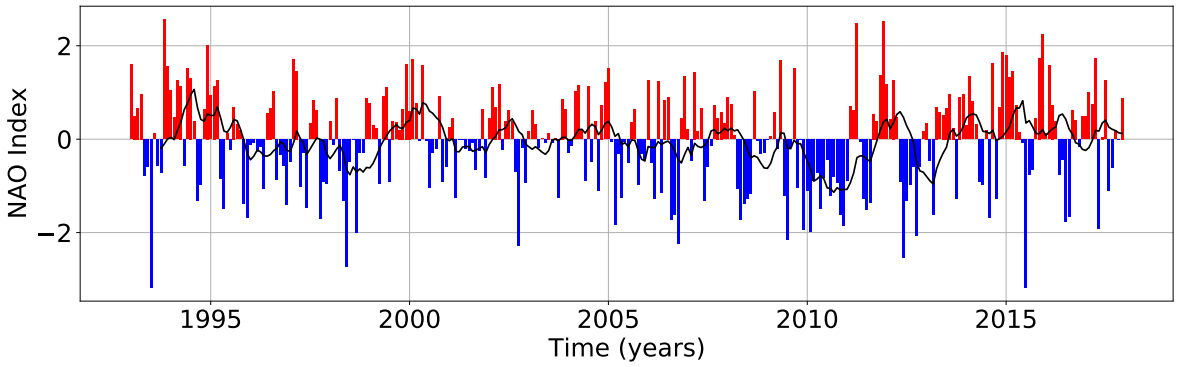

(a) NAO Index, 1993-2017

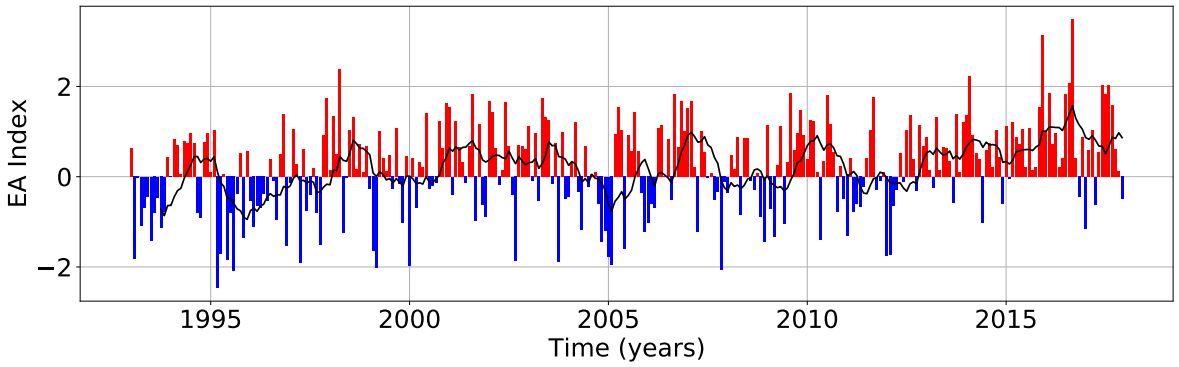

(b) EA Index, 1993-2017

Figure 2.4: NAO and EA index from 1993 to 2017. Positive (red) and negative (blue) NAO (a) and EA (b) pattern and the rolling mean for 10 month (black line, plot created in Python, data from NOAA, NAO: NOAA 2020b, EA: NOAA 2020a).

low pressure system propagating from the north Atlantic to the western United Kingdom (EA+, Barnston and Livezey 1987). During opposite phases of the NAO and the EA, the NAO migrates to the southwest changing the strength of the dipole and modulating the Azores High which can lead to more extreme weather conditions (Bastos et al. 2016, Kalimeris et al. 2017). Thus, these changes in the wind conditions during positive and negative NAO years and especially during coupled phases with the EA affect the transport of heat and water vapor throughout the European continent and the Atlantic Ocean (Bastos et al. 2016, Häkkinen 1999, Yamamoto et al. 2020, Yan et al. 2004). This makes it important to consider the NAO and its coupled, opposite phases with the EA in the current study. As the signals are strongest in winter, the averages of December to March will be used (Barnston and Livezey 1987, Cropper et al. 2014, Gómez-Letona et al. 2017,

Levitus et al. 2000, Pardo et al. 2011, Santos et al. 2005).

Even though, the El Niño-Southern Oscillation (ENSO) and the Pacific Decadal Oscillation (PDO) originating in the Pacific Ocean are known to affect the north Atlantic Ocean through teleconnection patterns (Enfield and Mayer 1997, García-Serrano et al. 2017), they will not be addressed further due to ambiguous results in previous studies. Roy and Reason (2001) and Enfield and Mayer (1997) found a possible relationship between ENSO and changes in the trade winds and upwelling in the region with a time lag of four to five month. Contrary to that, previous studies by Cropper et al. (2014) and Narayan et al. (2010) were not able to detect any significant correlations in regards to the upwelling activity in the Canary Current.

3 Data and Processing

The data used for the current study was obtained from different data sources and processed using several methods which will be addressed in the following section. Table 3.1 gives an overview of the data sets used for the different objectives defined for the study. All data processing was done using Python. Additionally, QGIS was used to display the data in maps.

Objective	Used data set(s)
Upwelling	(WOA18,) GREP, ERA5, PFEL
Vertical structure	(WOA18,) GREP
Climate Patterns	NOAA

Table 3.1: Overview of the used data sets for the different objectives of the study. Refer to text for abrrevations, data sources and processing methods.

3.1 In-situ Data from the World Ocean Atlas 2018

One of the main aims of the study was the sole usage of in-situ data to obtain precise results about the real conditions in the upper ocean and its variability with up- and downwelling as well as with the different climate patterns. The World Ocean Atlas (WOA18, Locarnini et al. 2019, Zweng et al. 2019, NOAA 2019) of the National Oceanic and Atmospheric Administration (NOAA) provides measurements taken by cruises between 1969 and 2019. The in-situ data for temperature and salinity was downloaded and processed to make predictions about their usability for this study.

In order to evaluate the influence of upwelling on the vertical structure of the ocean, near- and offshore areas were defined using the 200 meter isobath and variable grids offshore. The selection of the latitudes was done using 1°grids from 25 to 35°N. For the longitudes 0.5°grids between -30 to -6°W have been chosen depending on the coastline orientation using the distance of 500 km offshore as a guideline, however, at 25.5°, a lower distance has been selected to include the amount of profiles in the proximity of the 500 km line. As upwelling is detected in cross-shore sections within the same latitude and time (section 2.4), the location of all available vertical profiles throughout the years have been plotted in QGIS (fig. 3.1).

In a next step, all the profiles meeting the following criteria have been selected: (i) Same latitudinal range (1°steps), (ii) same time (month) and (iii) at least one profile simultaneously available

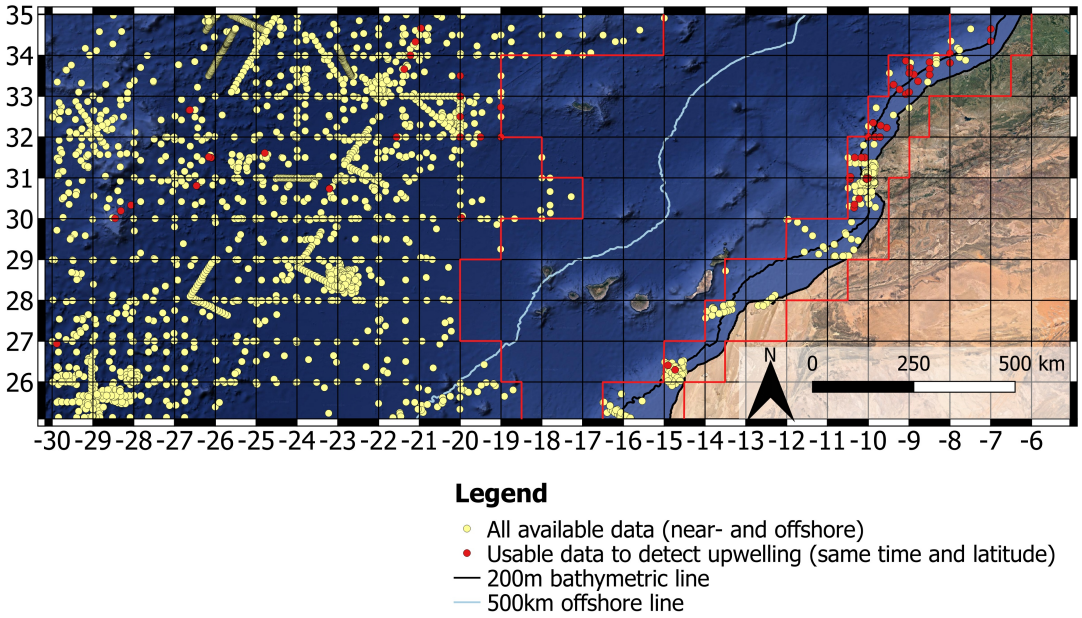

Figure 3.1: Available data from the WOA18. Map of the study area showing all available data (light yellow dots) from the WOA in the nearshore area (grids containing the 200 m isobath, framed by red lines at the coast), the 500 km offshore line and the offshore area (longitudes chosen considering the islands, red line), as well as the data available for the same time and 1°latitudinal range (red dots indicate available data nearshore and offshore for the same latitude and month, map created in QGIS using the data from the WOA18 by NOAA 2019).

in the defined near- and offshore area. Figure 3.1 shows the measurements which meet the criteria (red dots) along with the total number of available data in the WOA18 (light yellow dots). As each red dot only represents one available profile, the lack of available data for the purpose of the study made it necessary to use another data source (see 3.2).

3.2 Reanalysis Data from Copernicus (GREP)

The Global Ocean Ensemble Physics Reanalysis (GREP, PHY_001_026) is provided by the E.U. Copernicus Marine Service Information (Copernicus Monitoring Environment Marine Service: CMEMS, E.U. Copernicus Marine Service Information 2020). The Global Ocean Ensemble Physics Reanalysis (GREP) data is produced using a numerical model (NEMO model on ORCA025 grid, Bernard et al. 2006) with a surface forcing by ERA interim and data assimilation using satellite and in-situ data. For the PHY_001_026, a homogeneous 3D horizontal grid is available for the global ocean for a period of 1993 to 2017 which also offers information about

the vertical structure of the ocean in 75 depth levels up to a total depth of 5,500 m (resolution: 10 m at 100 m depth, increasing up to 200 m towards the bottom, Desportes et al. 2017). Besides the latitudinal and longitudinal data, the data set contains six variables for each, potential temperature and salinity. These monthly mean data (global-reanalysis-phy-001-026-grepv1-monthly) is provided by four different production centers: Mercator Océan in Toulouse, France (GLORYS2V4, variables: so_glor and thetao_glor, Lellouche et al. 2013), UK Met Office (FOAM-GLOSEA5v13, variables: so_foam and thetao_foam, MacLachlan et al. 2015, Blockley et al. 2014), CMCC, Italy, (C-GLORS, variables: so_cglo and thetao_cglo, Storto et al. 2016), and ECMWF (ORAS5, variables: so_oras and thetao_oras, Zuo et al. 2017). From these four sources, the overall mean (variables: so_mean and thetao_mean) as well as the standard deviation (variables: so_std and thetao_std) was calculated and provided in NetCDF-Format on a FTP server (Copernicus Monitoring Environment Marine Service 2020). For all computations and plots of the current study, the provided mean values of the salinity and the potential temperature have been used.

By comparing the GREP data to in-situ measurements, Desportes et al. (2017) found small errors in the GREP mean (> 0.1°C on global average) with the greatest disagreement in the data sets from 1993 to 2002 and in deeper layers below 800 m depth. After the deployment of Argo buoys in 2002, the data quality of the upper layer improved. The authors also detected overall fresher water (global average > 0.02 psu and > 0.1 psu between 50 and 800 m depth), however, besides the Mediterranean Sea Outflow, the greatest discrepancies occur in regions outside of the selected study area in the CCUS.

3.3 Computation of Upwelling Indices

Upwelling Indices were computed in Python using different approaches and data sets. The obtained UI data sets have been normalized using an unity-based normalization (Gajera et al. 2016, Lu et al. 2019).

3.3.1 UI based on Sea Surface Temperature

In order to obtain the Upwelling Index based on SST (UI_{SST}), the GREP reanalysis data was used (E.U. Copernicus Marine Service Information 2020). From the data set, the mean potential temperature of the shallowest available depth (0.50576 m) was extracted and, considering the coastline orientation, grouped into near- and offshore areas (tab. 3.2). For both groups, the mean potential temperature has been calculated for each latitude. As a result, the $SST_{inshore}$ value contains all grid cells between the coastline and the 200 m isobath and the $SST_{offshore}$ all grids below the variable line considering the islands to -40.5°W. For each 1°latitudinal step, the mean nearshore potential temperature was subtracted from the mean offshore potential temperature to obtain the UI_{SST} and, therefore, up- and downwelling events according to equation 1 (ch. 2.4).

Latitude (°N)	**Longitudinal Range Offshore (°W)**	**Longitudinal Range Nearshore (°W)**	
	Smaller than	Start	End
25.5	-19.0	-16.5	-15.5
26.5	-19.0	-14.5	-14.5
27.5	-20.0	-13.5	-13.5
28.5	-20.0	-13.5	-11.5
29.5	-19.0	-11.5	-10.5
30.5	-17.0	-10.5	-10.5
31.5	-18.0	-10.5	-10.5
32.5	-19.0	-9.5	-9.5
33.5	-19.0	-9.5	-8.5
34.5	-15.0	-7.5	-7.5

Table 3.2: Definition of the near- and offshore area for the calculation of upwelling. Selected grids used to calculate upwelling using the Copernicus and ERA5 data (see also fig. 3.1: red line/squares, adapted).

3.3.2 UI based on Wind Data

For upwelling based on wind two different data sets were used: the fifth global version of the European Centre for Medium-Range Weather Forecasts (ECMWF) Re-Analysis data (ERA5, UI_{ERA5}) and the Pacific Fisheries Environmental Laboratory (PFEL, NOAA Fisheries 2019), a service provided by the NOAA (UI_{PFEL}).

The ERA5 data is available on the Climate Copernicus website (ECMWF Copernicus 2019).

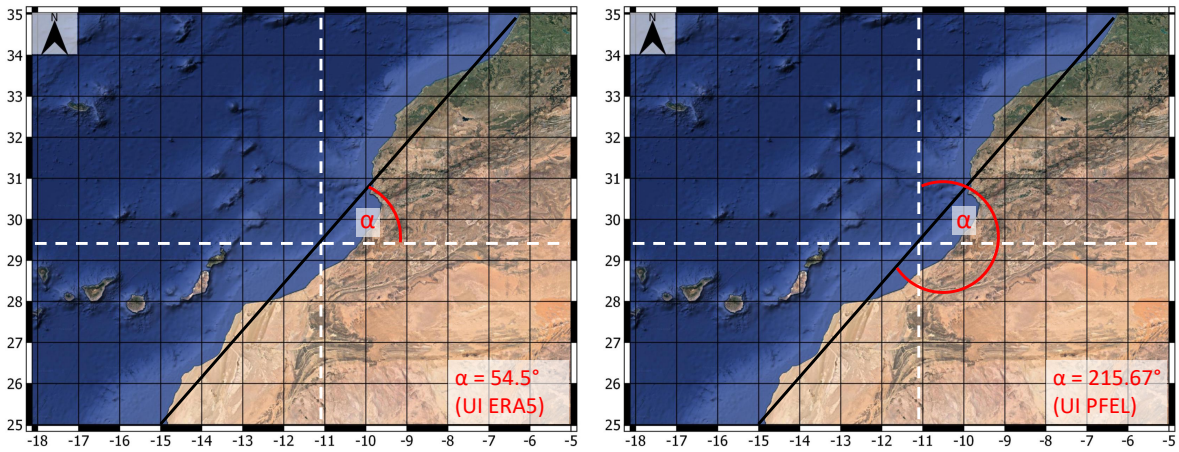

(a) ERA5 **(b)** PFEL

Figure 3.2: Coastline geometry and orientation considered for the UI_{ERA5} and UI_{PFEL}. Angle of the coastline (α) for the UI_W based on ERA5 (a, Cropper et al. 2014) and PFEL (b, Bakun 1973 and 1975, NOAA Fisheries 2019).

From this website, the monthly reanalysis data was downloaded in a 0.25°grid for the years 1979 to 2019 and adapted to the time frame of the GREP data (1993-2017). Using the zonal and meridional component of the wind speed ($\vec{u}$ and $\vec{v}$), the Ekman transport and the resulting up- and downwelling events were calculated using the equation provided by Cropper et al. (2014) and the coastal orientation of the mean coastline (fig. 3.2a, see eq. 2-4, ch. 2.4). The index was resampled to 1°grid cells to simplify the comparison with the UI_{SST}.

In order to verify the results of the calculated UI_{ERA5}, the data from PFEL (NOAA) was downloaded from the Environmental Research Division Data Access Protocol server (NOAA ERDDAP 2019). The data set provides the results for the zonal and meridional component of the Ekman transport and allows the computation of the Upwelling Index in consideration of the prevailing coastline geometry using a function for Python which is also provided by NOAA (fig. 3.2b). The results give the water advection sea- (upwelling) and shoreward (downwelling) in cubic meter per second per 100 m (Menge and Menge 2013, Miller and Shanks 2004, NOAA Fisheries 2019).

3.4 Ocean Stratification

As the GREP data only provides potential temperature and salinity values, the density (ρ) has been computed for each depth using the Gibbs Seawater (GSW) toolbox for the Thermodynamic Equation of Seawater - 2010 (TEOS-10, McDougall and Barker 2011). Firstly, the pressure was calculated using the gravity of the earth ($g = 9.8ms^{-2}$) assuming a constant change with depth. In a next step, the density was computed using potential temperature (θ), salinity and the pressure.

The depth of the surface layer was computed based on the potential temperature data (= isothermal layer depth) using the difference criterion with a fixed value of 0.8°C and a reference level of 9.82 m. The resulting ILD marks the depth before the potential temperature is 0.8°C or more lower than the temperature at the reference level. The temperature gradient of 0.8°C is widely used in recent studies and lead to the best results for the profiles used in this study (Chu and Fan: 2010 and 2011, Kara et al. 2000). For the reference depth, the closest available depth of the GREP data to the commonly used 10 m depth reference was chosen. As de Boyer Montégut et al. (2007) found a small thickness of the barrier layer in the region of the study area and there is no freshwater input along the coastline causing a barrier layer (Arístegui et al. 2009) the same depth have been used for ILD and MLD (ch. 2.3).

The vertical profiles have been extracted from the 4D GREP grid for all up- and downwelling events in the study area. The events of all latitudes were grouped and all profiles of the same month plotted in one figure. For the nearshore area, the events have been plotted as single profiles whereas the high amount of offshore profiles (115 profiles/grid cells including all between 25.5 to 35.5°N and the ones defined in tab. 3.2 down to -40.5°W) is only shown in an envelope. For the latter, using all available offshore profiles, the minimum, mean and maximum values per depth was computed and only this extracted range plotted for reasons of clarity. Additionally, the mean ILD for the extracted month has been plotted in the profiles. The summer (JJAS) and winter (DJFM) means of the ILD has also been calculated for years where upwelling was not detected using the defined thresholds to compare its changes with up- and downwelling events. For this neutral UI, threshold values of >-1 and <5°C has been selected for the UI_{SST} and >-0.4 and <1.5 for the UI_{ERA5}. As the obtained values are similar for both UI's, the mean of both have

been computed for summer and winter months.
Outlier in the vertical profiles have been detected visually for the nearshore area since the usage of automated approaches in Python has not lead to good results.

3.5 Composite Maps

Composite maps have been created in order to analyze the correlation between upwelling indices with the vertical structure of the potential temperature (θ) and between the climate pattern and the horizontal structure of the potential temperature. The composite plots are obtained by summing plots of positive and negative events, respectively.

3.5.1 Upwelling Indices and Ocean Stratification

For the UI_{SST}, thresholds of +5°C and -1°C have been used to determine the positive and negative groups of events in the time series and the mean temperature values of all detected events for each latitude have been calculated to plot the composite maps. The threshold for the UI_{ERA5} was set to 1.5 and -0.4. In order to analyze the vertical structure of the ocean during up- and downwelling events, the composite maps have been plotted as vertical slices along the latitudes up to a depth of 300 m.

3.5.2 Climate Indices

The data used for the NAO and the EA was downloaded from the Climate Prediction Center of NOAA (2020a and 2020b). For both, the NAO and the EA, the study period (1993-2017) has been extracted and extended winter means for the months December to March computed (DJFM, Hurrell et al. 2003, Martínez-Asensio et al. 2016). Additionally, summer means from June to September (JJAS) have been calculated to investigate possible influences on the summer ILD and upwelling which occurs during summer month in the selected study area. A threshold of 0.5 and -0.5 has been used to determine positive and negative events, respectively. For the NAO, the mean potential temperature values of all positive and negative events has been computed using the GREP data. The same was done for coupled, opposite phases of the NAO and the EA index (NAO+EA-/NAO-EA+). These phases have then been used to extract and plot the winter

means (DJFM, except for 1993: January to March only) in composite maps (Bastos et al. 2016, Iglesias et al. 2017, Martínez-Asensio et al. 2014, Neves et al. 2019). Horizontal slices of the mean potential temperature at four different depths (0.5, 47.21, 97.04, and 199.79 m) have been plotted according to the calculated ILD with the exact depths being dependent on the available depth steps of the GREP data.

3.6 Correlations and Trends

The relationship of all data sets has been tested using the Pearson correlation coefficient (Benesty et al. 2009, Pearson 1895, Rodgers and Nicewander 1988) and a significance level of 0.05 ($p < .05$, Gómez-Letona et al. 2017).

For the study, the calculated upwelling indices have been correlated with each other as well as the near- and offshore ILD and the UI's with the ILD. Additionally, these data sets (UI's and ILD) were correlated with the climate patterns (NAO and EA).

The analysis of trends in the time series has been restricted to the linear regression model as it plays a minor part in this study.

4 Results

The results of the study will be described in the following section. The interpretation will be done separately in the next chapter.

4.1 Upwelling Indices

Upwelling was calculated using three different data sets and approaches. The UI_{SST} and the UI_{ERA5} was calculated using the equations 1-4 (ch. 2.4). Additionally, the UI_{PFEL} was determined using data and a function for Python provided by NOAA.

The calculation of the upwelling events leads to different results depending on the data and its processing. Figure 4.1 shows the time series plots of each index separated by latitude (single

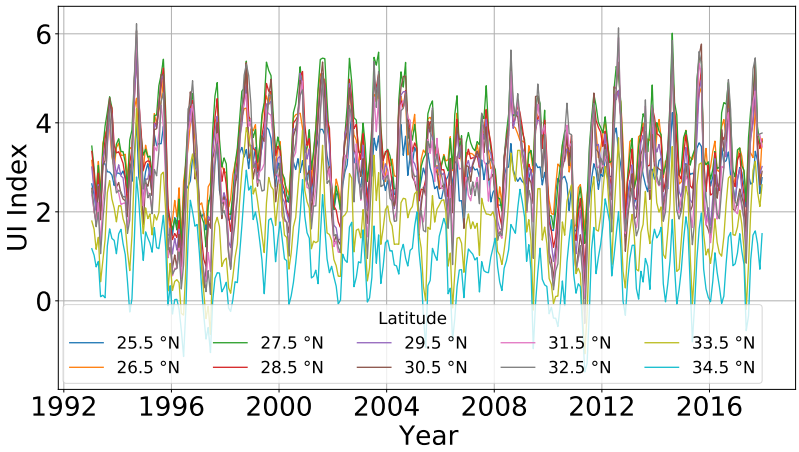

(a) UI based on SST data (GREP, PHY_001_026)

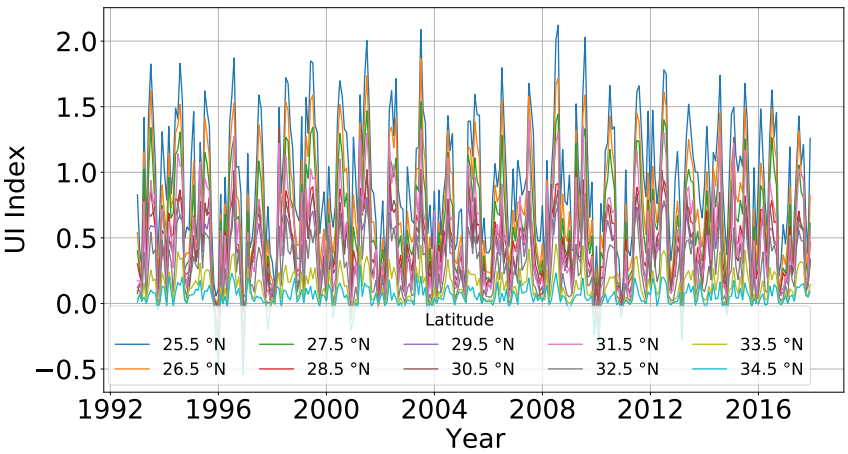

(b) UI based on ERA5 (ECMWF, 1°grid)

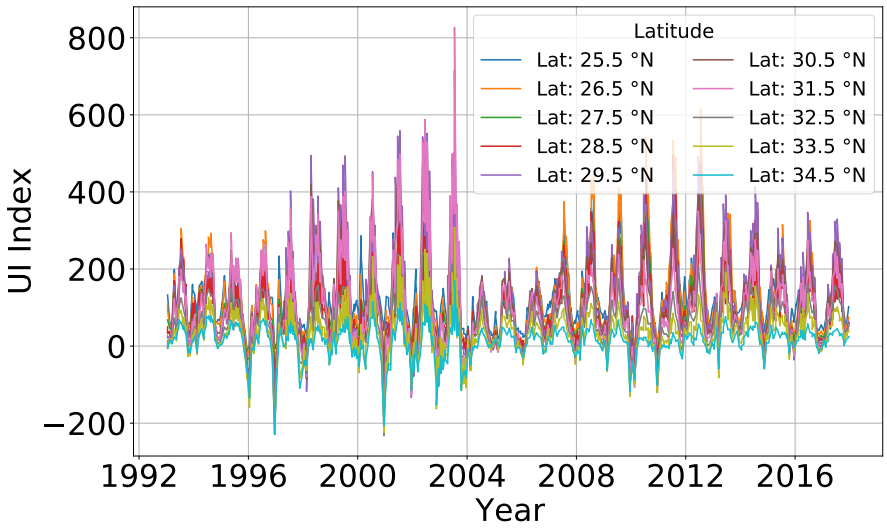

(c) UI based on PFEL (NOAA)

Figure 4.1: Time series plot of the Upwelling Indices per latitude. Plots showing the variation of the calculated upwelling indices (SST (a), ERA5 (b), and PFEL (c) data) for each latitude (plots created in Python, data obtained from E.U. Copernicus Marine Service Information 2020: SST of GREP, ECMWF Copernicus 2019: ERA5, and NOAA Fisheries 2019: PFEL)

plots for each latitude see fig. A.1, A.2, and A.3, appendix). All indices reveal mostly positive values (upwelling) in different magnitudes and with different spreads in their spatial and temporal extent. There is a clear annual cycle in all of the indices with higher index values during the summer and autumn months. The strength of the indices varies with the latitude. In the UI_{SST} and the UI_{PFEL}, the middle latitudes of the study area (27.5-30.5°N) reveal highest values (fig. 4.1a and 4.1c) whereas values of the UI_{ERA5} decrease with increasing latitudes (fig. 4.1b). The lowest values in all UI's can be found in the highest latitudes.

Calculating the temporal trend using the linear regression, the UI_{SST} and UI_{ERA5} show both, small positive and negative tendency depending on the latitude (fig. A.1 and A.2, appendix) whereas the UI_{PFEL} implies a small positive tendency towards more upwelling events (exception: latitude 31.5°N, see fig. A.3, appendix). All trends are, however, small in either direction with a slope between -0.02 and 0.1.

The normalized data of all UI's has been plotted in a grouped boxplot showing its distribution per latitude. All UI's reveal an uni-modal distribution with the UI_{SST} data being spread widest and the UI_{ERA5} and UI_{PFEL} data slightly negatively skewed. The boxplot confirms the results of

the time series: The highest index values of the UI_{SST} occur around 27.5°N, of the UI_{PFEL} up to 31.5°N, and of the UI_{ERA5} data at 25.5°N followed by decreasing values with increasing latitude (except at 30.5 and 31.5°N, fig. 4.2a).

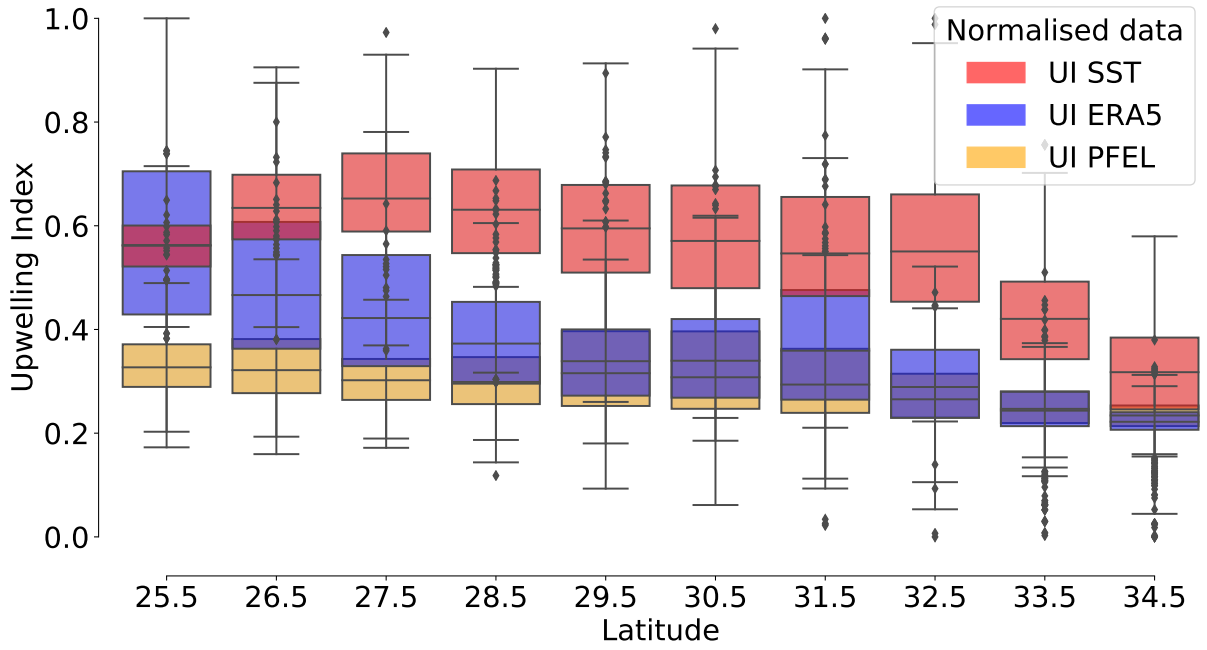

(a) Comparison of the distribution of all UI's (normalized)

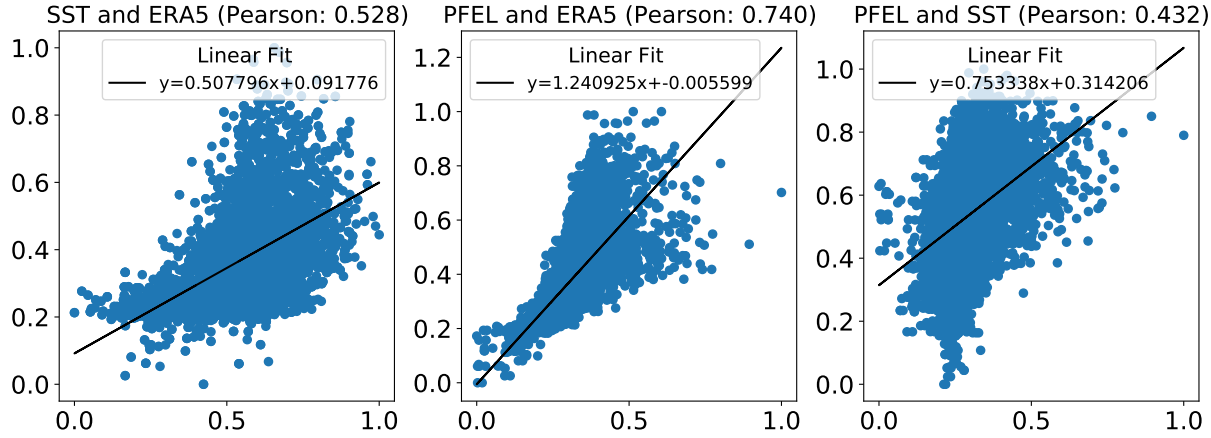

(b) Scatter plots indicating the correlation of all UI's

Figure 4.2: Correlation of all selected Upwelling Indices. Distribution of the UI data along the latitude (a, normalized data) and the correlation of the indices (b, Pearson's correlation coefficient in the title of each plot, plots created in Python, data obtained from Copernicus Monitoring Environment Marine Service 2020: SST of GREP, ECMWF Copernicus 2019: ERA5, and NOAA Fisheries 2019: PFEL).

The correlation between the UI's differ (fig. 4.2b). Since the UI_{ERA5} and the UI_{PFEL} are based on wind data, there is, as expected, a higher degree correlation between them (Pearson's correlation coefficient: 0.74). Between the UI_{SST} and UI's based on wind (UI_{ERA5} and UI_{PFEL}), a moderate correlation has been detected (0.528 and 0.432). All correlations between the UI's are significant ($p < .0001$). For all further processing methods, only the UI_{SST} and the UI_{ERA5} have been used. The UI_{PFEL} has been neglected as its calculation is less transparent compared to the others.

4.2 Ocean Stratification

The results for the upper ocean structure will be addressed for each processing method in the following section.

4.2.1 Vertical Composite Maps of the Up- and Downwelling Events

In order to analyze the vertical structure of the up- and downwelling events, all months with positive or negative events have been extracted from the time series for each latitude. Depending on the selected UI and the defined thresholds of <-1 and >5°C (UI_{SST}) and <-0.4 and >1.5 (UI_{ERA5}), respectively, the events occur on a different temporal and spatial scale. Using the dates of these events, vertical composite maps of the potential temperature have been built by calculating the sum of the events per latitude for both indices and the results have been plotted. In order to assess the vertical structure of up- and downwelling events as well as its changes with the latitude, a lower, middle and upper latitude has been selected. Since upwelling has only been detected between 26.5 and 32.5°N in the UI_{SST} time series, the vertical composite map at 26.5°N along with the one at 30.5°N has been plotted. For the UI_{ERA5}, upwelling was detected at 25.5, 26.5, and 27.5°N with the defined threshold. Due to their proximity to each other, only one composite (25.5°) is shown.

Downwelling became apparent at 33.5 to 34.5°N in the data set of both indices and, additionally, at 32.5°N in the UI_{ERA5}. Therefore, the vertical composite for downwelling has been plotted along the highest latitude of the study area (34.5°N) for both UI's.

For 26.5°N of the UI_{SST} (fig. 4.3a), three events have been determined to exceed the threshold of 5°C and the sum of these events has been calculated and plotted. The composite map shows

higher potential temperatures at the surface farther offshore (<-30°W) and a decrease of the potential temperature towards the coast. The same trend can be observed throughout all depths and at 30.5°N (fig. 4.3b) where 14 events (months) exceeding the threshold of >5°C have been summed and plotted. The isotherms are closer to each other at the surface in the offshore area with an increasing space between them with depth and towards the coast.

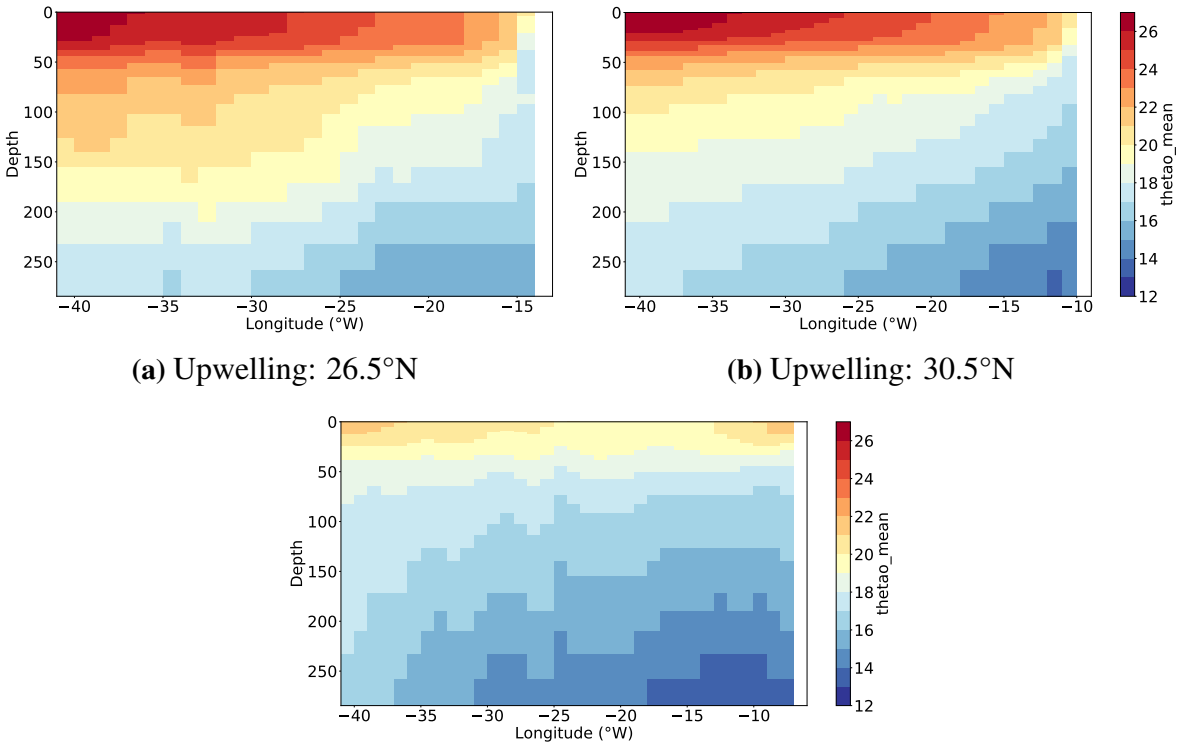

(a) Upwelling: 26.5°N

(b) Upwelling: 30.5°N

(c) Downwelling: 34.5°N

Figure 4.3: UI_{SST}: Vertical composite maps for selected latitudes. Plots showing sums of dates where the threshold of -1 and 5°C was exceeded revealing the variation of the upper ocean structure along the longitudes for up- and downwelling events (plots created in Python, data obtained from E.U. Copernicus Marine Service Information 2020).

The composite for downwelling of the UI_{SST} at 34.5°N (fig. 4.3c, sum of 6 months) reveals a different distribution of the potential temperature throughout the section. In the upper layers down to a depth of around 100 m, the isotherms are almost parallel to the surface with an exception at the coast and the offshore area around -40°W where the potential temperatures are slightly higher than in the section between them. The spaces between the isotherms are smaller at the surface and almost parallel to it. Again, they are increasing with the depth and towards the coast, however, this signature is apparent up to -12.5°W. From there towards the coast, the

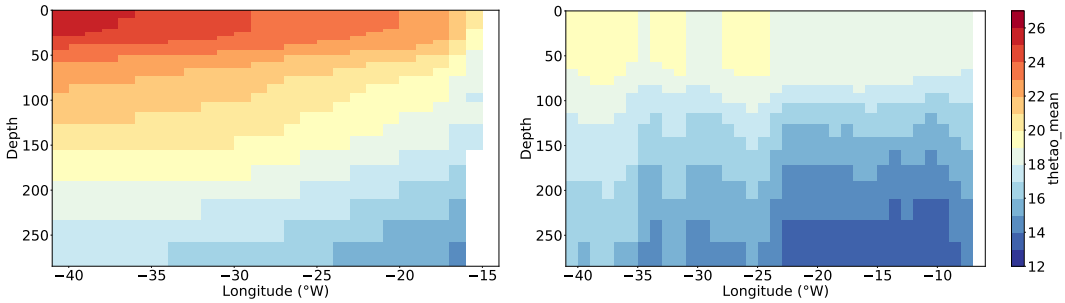

(a) Upwelling: 25.5°N **(b)** Downwelling: 34.5°N

Figure 4.4: UI_{ERA5}: Vertical composite maps for selected latitudes. Plots showing sums of dates where the threshold of -0.2 and 1 was exceeded revealing the variation of the upper ocean structure along the longitudes for up- and downwelling events (plots created in Python, data obtained from E.U. Copernicus Marine Service Information 2020, and ECMWF Copernicus 2019).

isotherms decrease again below 100 m depth.

The UI_{ERA5} shows a similar distribution of potential temperature for the upwelling events where the sum of 38 events has been calculated (fig. 4.4a). The isotherms reveal a gradient from the surface of the offshore area towards the depth at the coast as detected in the upwelling events for the UI_{SST}. Again, there is a slope towards the surface of the coastal area, however, the isotherms are more equally spaced throughout the whole section (fig. 4.3a and 4.3b). Contrary to the UI_{SST}, the UI_{ERA5} composite for downwelling events at 34.5°N (two month) has a different signature. Even though, the isotherms are also parallel to the surface, the potential temperature is almost constant in the upper 50 to around 100 m of the section. Throughout the depth, sharp transitions in the parallel structure of the isotherms become visible at around -25 and -35°W which distinguishes the vertical structure in the deeper layers of both UI's from one another. Still, both UI's show a downward slope at the coast (>-10°W) below 100 m depth and generally cooler potential temperatures compared to the upwelling composites with warmer water in the offshore area compared to the nearshore waters during downwelling events (fig. 4.4b and 4.3c).

4.2.2 Vertical Profiles of Up- and Downwelling Events

Vertical profiles for both, up- and downwelling events have been plotted using the GREP data. The defined threshold of 5°C for upwelling and -1°C for downwelling has lead to the detection of 29 month with up- and six month with downwelling in the UI_{SST} values (see ch. 3.5.1).

Upwelling occurs in summer and autumn (July to November), however, the most intense events are in August and September. Downwelling occurs in May and June (tab. 4.1).

Event	Latitudes	Month	Occurrence
Upwelling	25.5-32.5°N	July	5
		August	11
		September	9
		October	2
		November	2
Downwelling	33.5-34.5°N	May	1
		June	5

Table 4.1: Occurrence of up- and downwelling events per month. Summary of all detected events of the UI_{SST} (Upwelling >5°C, Downwelling <-1°C).

For the UI_{ERA5}, a threshold of 1.5 and -0.4 was used, leading to 38 month for up- and two for downwelling. Upwelling occurs mostly in July (30x) and August (16x) but also in April (3x), June (5x) and September (1x) whereas downwelling was only detected in January and December of 1996.

Depending on the selected events, vertical profiles for the UI_{SST} and the UI_{ERA5} have been extracted and plotted. The events of all latitudes exceeding the defined thresholds in a given month have been grouped and plotted in one figure. While single profiles are shown for the nearshore area, the high number of offshore profiles (115 profiles/grid cells, see ch. 3.4 and tab. 3.2) have been plotted in an envelope showing only the minimum, mean and maximum values of each depth for reasons of clarity. In order to see the variation of the vertical profiles with time, two months have been selected for both events and both UI's at the beginning and towards the end of the selected time span depending on their availability. The profiles for January and December of 1996 have been plotted to show downwelling detected in the UI_{ERA5}.

The vertical profiles for upwelling all reveal lower temperatures and higher density values in the nearshore area (fig. 4.5). Compared to the envelope plotted for all available offshore profiles, the nearshore values are below (pot. temperature) and above (salinity) the offshore values up to a depth of 100-150 m. Below that depth, the differences in potential temperature and density between the near- and offshore area vanish, however, the values remain below and above the mean offshore values, respectively (fig. 4.5a and 4.5b).

The mean potential temperature at the surface near in the nearshore area is around 20°C, whereas

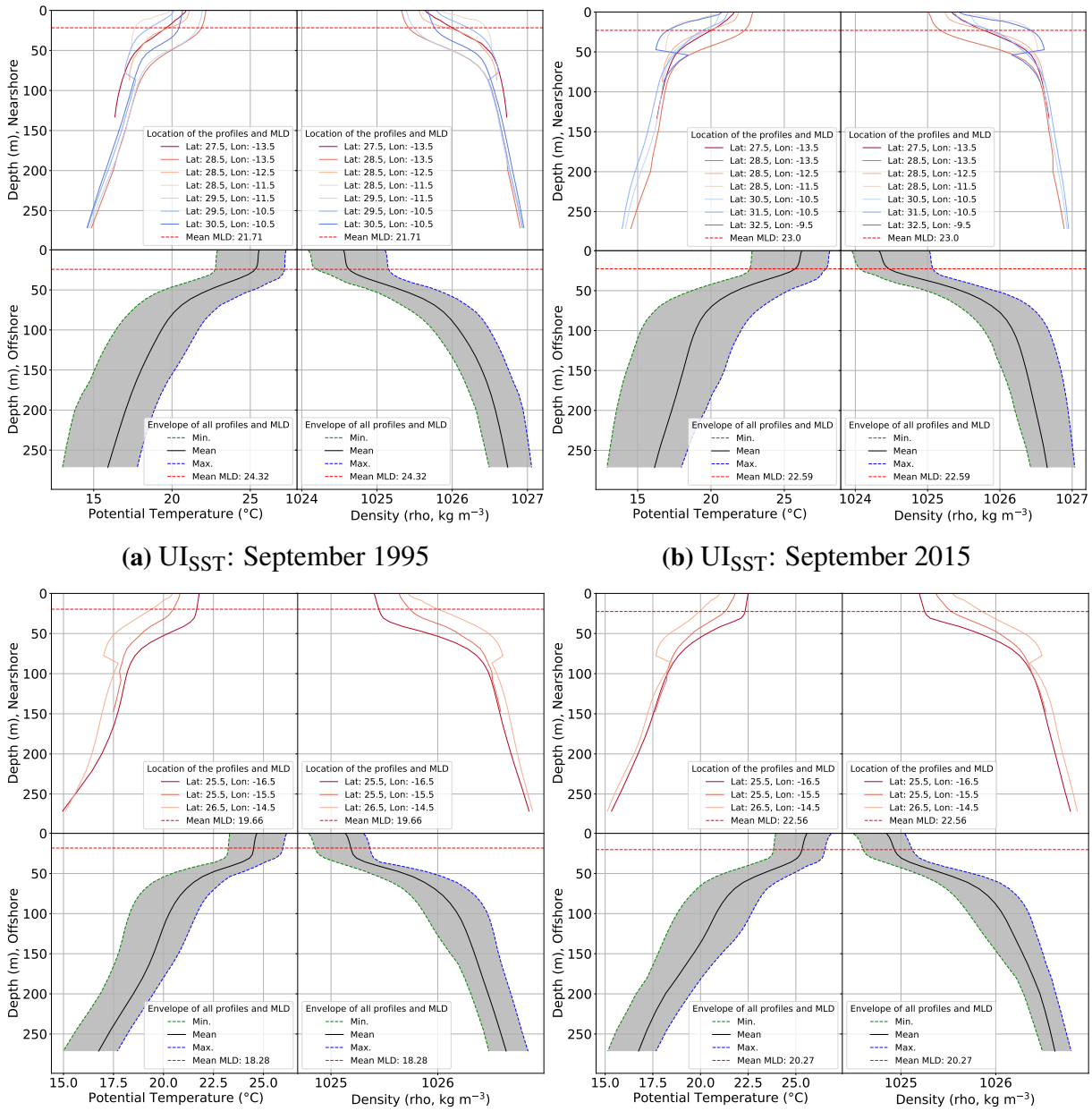

(a) UI_{SST}: September 1995

(b) UI_{SST}: September 2015

(c) UI_{ERA5}: August 1994

(d) UI_{ERA5}: August 2012

Figure 4.5: Vertical Profiles of upwelling events. Plot of the GREP data for the nearshore (upper) and offshore (lower, envelope of minimum, mean, and maximum values) area as well as the mean location of the ILD for the UI_{SST} (September 1995 (a) and 2015 (c)) and the UI_{ERA5} (August 1994 (c) and 2012 (d), plots created in Python using E.U. Copernicus Marine Service Information 2020 data).

offshore it is around 25°C in the profiles of both UI's. The isothermal and mixed layer as well as the thermo- and pycnocline are well defined with the maximum depth of the thermocline

marking the transition of both areas, near- and offshore, and the alignment of both (at 100-150 m). The mean isothermal layer depth is around 23.23 m nearshore and 22.88 m offshore for the UI_{SST}. The UI_{ERA5} has a deeper ILD of 27.74 m at the coast and lower one of 24.09 m offshore. The calculated ILD fits less well in the profiles of the UI_{ERA5}, even though, the same fixed value was used for the difference criterion (see ch. 3.4). In comparison to years of a neutral UI (UI_{SST}: index values of >-1 and <5°C, UI_{ERA5}: index values of >-0.4 and <1.5), the mean ILD for summer month (JJAS) is at 22.2 m at the coast and 20.4 m offshore for both UI's (tab. 4.2 and ch. 3.4). Therefore, the results imply a deepening of the ILD with upwelling events which is more distinct in the nearshore area UI_{ERA5} events.

Event	Upwelling Index	Nearshore ILD (m)	Offshore ILD (m)
Upwelling	UI_{SST}	23.23	22.88
	UI_{ERA5}	27.74	24.09
Summer Means (JJAS)	Neutral UI's	22.2	20.4
Downwelling	UI_{SST}	19.97	18.85
	UI_{ERA5}	80.6	84.78
Winter Means (DJFM)	Neutral UI's	98.9	99.8

Table 4.2: Variation of the ILD with up- and downwelling. Mean ILD for up- and downwelling event for each UI as well as the mean ILD for years of neutral indices.

Contrary to the upwelling profiles, the vertical profiles extracted for downwelling events for both UI's are vary a lot. While all profiles are within the computed range of the offshore profiles or, for the UI_{ERA5}, just slightly below/above them (fig. 4.6), the depth of the isothermal layer differs. For the UI_{SST} profiles, the mean ILD is 19.97 m nearshore and 18.85 m offshore. The ILDs for the UI_{ERA5} are strikingly deeper with a mean of 80.6 m at the coast and 84.78 m offshore. The ILD in the winter month (DJFM) for neutral years of both UI's is 98.9 m at the coast and 99.8 m offshore. Therefore, the ILD is shallower during downwelling. The big difference between the winter ILD of the neutral UI's and the downwelling events of the UI_{SST} is rather due to the timing than to the different calculation method of the UI's. As downwelling was detected in May and June using the UI_{SST} threshold of <-1°C, the ILD needs to be compared to the summer ILD of neutral years. Still, the ILD of the UI_{SST} downwelling events is shallower than the summer means calculated for neutral years.

The surface temperatures vary between 18 and 20°C for both UI's and both areas. The vertical

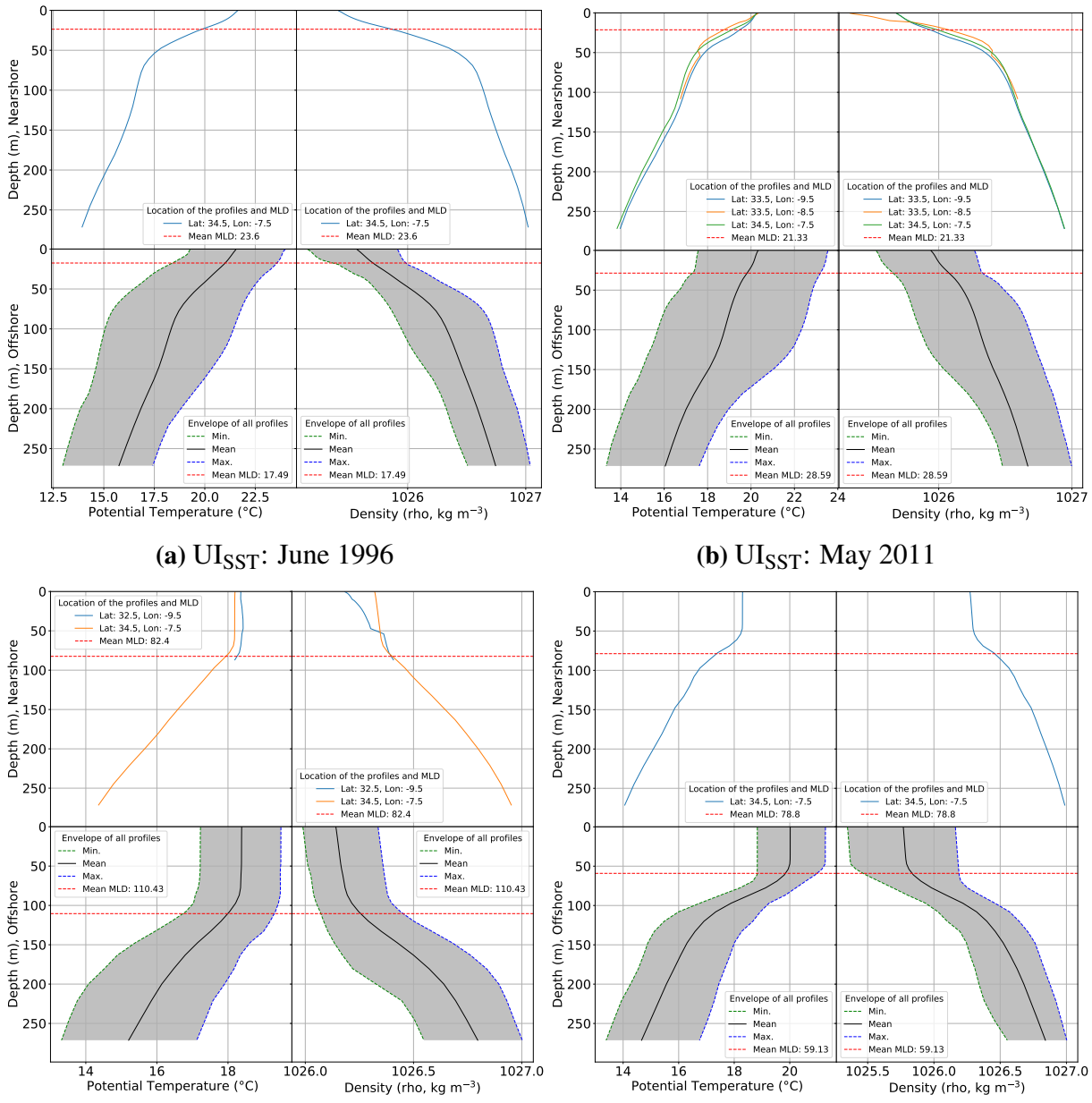

(a) UI_{SST}: June 1996

(b) UI_{SST}: May 2011

(c) UI_{ERA5}: January 1996

(d) UI_{ERA5}: December 1996

Figure 4.6: Vertical Profiles of Downwelling Events. Plot of the GREP data for the nearshore (upper) and offshore (lower, envelope of minimum, mean, and maximum values) area as well as the mean location of the ILD for the UI_{SST} (June 1996 (a) and May 2011 (c)) and the UI_{ERA5} (January (a) and December 1996 (b), plots created in Python using E.U. Copernicus Marine Service Information 2020 data).

profiles of both UI's show a less rapid change in the potential temperature and density in the upper meter of the profiles compared to the upwelling profiles. The ILD/MLD and thermo-/pycnocline are clearly visible.

Despite small variations in the potential temperature and density, there is no variation visible in the vertical structure on a temporal scale.

4.2.3 Isothermal Layer Depth

The ILD has been calculated using the GREP data and the difference criterion. The calculated depth corresponds to the depth step above the one where the potential temperature is 0.8°C cooler than the one at the reference depth of 9.82 m. The plots of the ILD time series (fig. 4.7) reveal an annual cycle for both, the near- and the offshore area. The deepest ILD for the whole time span of the study occurs in the winter month of each year where it is lower in the nearshore area at a depth of 199.79 meter in March 1994, 2012 and 2015 (all at 26.5°N) and deeper offshore with a maximum depth of 244.89 meter (March 2005 at 34.5°N). The shallowest nearshore ILDs of 9.82 m have been computed for summer and autumn (June to October) which is equal to the reference level. The same shallow depth can be observed in the offshore area in July of several years. Comparing the data sets, the offshore ILD shows a smaller spread between the latitudes and the maximum values of the ILD per year.

There is a high correlation coefficient of 0.75 between the whole time series of the near- and offshore ILD which is significant ($p < .0001$). Additionally, the winter (DJFM) and summer (JJAS) of the ILD time series have been extracted and the near- and offshore values correlated. The winter means do not show any correlation besides a strong one at 25.5°N (significant, $p <$

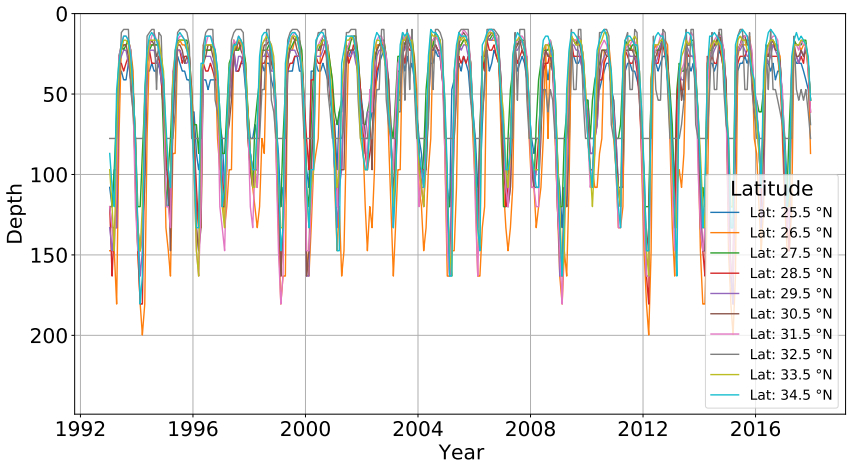

(a) Nearshore

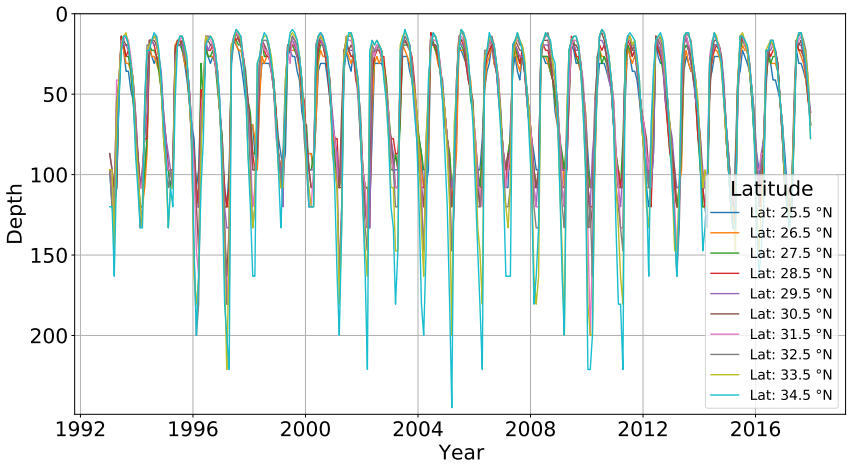

(b) Offshore

Figure 4.7: Time series of the isothermal layer depth per latitude. Isothermal layer depth calculated using the difference criterion (0.8°C) for the nearshore (a) and the offshore (b) area.

.009) but the summer means correlate significantly ($p < .0001$)

The Pearsons correlation coefficient has also been calculated for the full time series of the ILD and the different upwelling indices, however, the results show a negative weak to moderate but mostly significant correlation (-0.44 to -0.04, $p < .03$, see tab. A.1). Using a linear regression, the trend of the ILD over the whole time series has been calculated for each latitude. In general, the results do not show a trend, however, there is a small tendency towards a decrease in the ILD with time.

4.3 Climate Indices

As the NAO and the EA have their strongest signal during winter, December to March values have been extracted and the means calculated for each year. Using a threshold of -0.5 and 0.5 for a negative and positive index, respectively, 12 years of NAO+ and two of NAO- have been detected as well as two NAO+EA- and one NAO-EA+ (fig. 4.8). The timings of the events were used for the composite maps and for correlations between the climate patterns and both, the ILD and UI's.

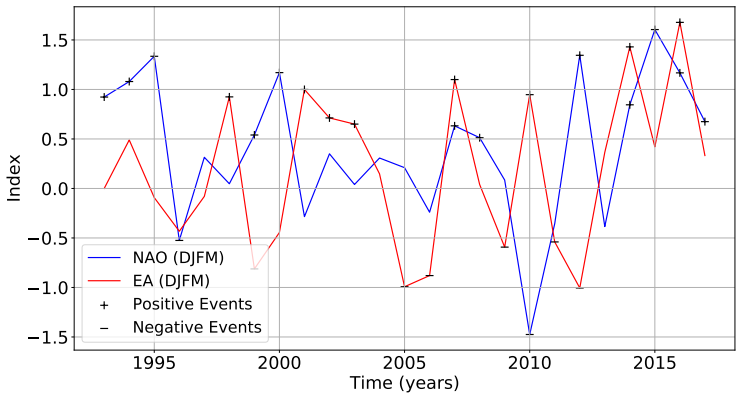

Figure 4.8: Time series of the winter means for the NAO and the EA. Winter averages of the climate indices, selected positive and negative phases of each mode marked with "+" and "-" (plot created in Python using data from NOAA: 2020a and 2020b).

4.3.1 Horizontal Composite Maps

Figure 4.9 shows the impact of the NAO and its coupled phases with the EA on the ocean stratification as horizontal sections of the potential temperature taken at different depths. Besides considering the potential temperature at the surface (0.5 m), different depth steps in the upper ocean have been chosen according to the calculated ILDs. The lowest depth of 199.79 m displays the conditions where the influence of the atmosphere through wind and heat flux is not present anymore.

The composite maps for all selected phases of the climate indices show a northeast to southwest gradient of the potential temperature for all depths. The lowest temperatures occur at the coast at 35°N and the highest offshore (-40°W) at the lower latitudes (25°N). In general, the potential

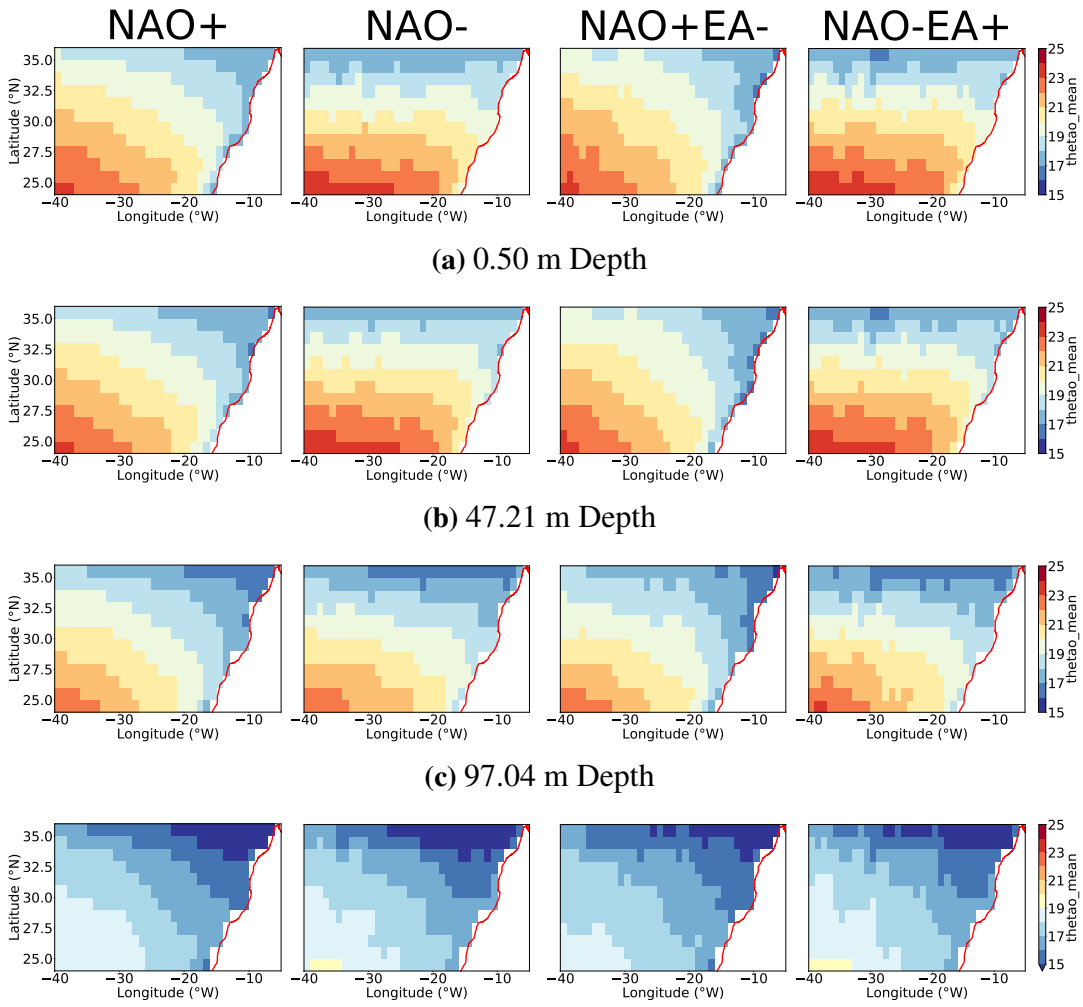

(a) 0.50 m Depth

(b) 47.21 m Depth

(c) 97.04 m Depth

(d) 199.79 m Depth

Figure 4.9: Impact of the NAO and the EA on the ocean stratification. Composite maps of NAO+, NAO-, and coupled NAO and EA phases for four depth steps: 0.5 (surface, a), 47.21 (b), 97.04 (c), and 199.79 m depth (d, plots created in Python using data from: NOAA: 2020a and 2020b, Copernicus Monitoring Environment Marine Service 2020, composite maps: Bastos et al. 2016, Iglesias et al. 2017, Neves et al. 2019).

temperatures along the coast are cooler than the ones offshore.

Considering the spatial distribution of the potential temperature with depth, the composite maps of NAO+ and NAO+EA- on the one hand and the ones for NAO- and NAO-EA+ on the other resemble each other. Both, the NAO- and the NAO-EA+ show an extent of similar potential temperature more parallel to the latitudes in the offshore area (longitude: -30 to -40°W) and, thus, an enhanced north-south gradient. This pattern is interrupted towards the coast where cooler water is found. The NAO+ and NAO+EA- both show a northeast to southwest gradient of the

potential temperature at the surface and colder water along the coast. In comparison to years of a negative NAO, the differences of potential temperature between near- and offshore are greater during years of NAO+ and NAO+EA- (fig. 4.9a).

Throughout the different depth steps, the temperature gradient stays the same for NAO+ and NAO+EA- years (northeast to southwest, fig.4.9b-4.9d, first and third composite) whereas during years of NAO- and NAO-EA+ water with a similar potential temperature extends further along the latitudes at 47.21 m (longitudes: -20/-25 to -40°W). The water in the nearshore area remains relatively cooler, however, the difference of the potential temperature between the near- and offshore area decreases (fig. 4.9b, second and fourth composite). The next selected depth (97.04 m) represents the transition zone of the sea-air interaction for all climate indices. While the ILD is lower than 97.04 m in the coastal area in NAO-/NAO-EA+ years, it is deeper offshore (tab. 4.3). Nevertheless, the composite at 97.04 m is similar to the one computed at the surface. For the NAO+ and NAO+EA- events, the ILD is inclined in the opposite direction. Therefore, the prevailing cooler potential temperatures at the coast coincide with the remaining influence of the isothermal layer.

At 199.79 m depth, the composites of all climate patterns show a northeast to southwest gradient in the potential temperature with a similar distribution for all four cases. Still, the contours of NAO-, NAO+EA- and NAO-EA+ have a more chaotic pattern.

Phase Climate Pattern	**Winter Means ILD (m)**		**Summer Means ILD (m)**	
	Nearshore	Offshore	Nearshore	Offshore
NAO+	104.25	96.71	22.18	20.68
NAO-	86.20	117.41	24.97	19.82
NAO+EA-	116.67	89.26	21.30	20.27
NAO-EA+	76.40	119.73	26.65	20.06
Neutral NAO	95.31	99.80	21.72	20.29

Table 4.3: Mean ILD (winter and summer) for the phases of the Climate Pattern. Mean ILD on the near- and offshore area for all years with detected positive, negative and coupled phases of the NAO and the EA and in neutral NAO years.

4.3.2 Correlation with Upwelling Indices and Isothermal Layer Depth

In order to establish possible relationships between the Climate Pattern and the UI's as well as the ILD, the Pearsons correlation coefficient and the level of significance has been calculated. The correlation between the winter means of the NAO and the UI_{SST} are all moderate being approximately 0.5 with a better correlation for the lower latitudes (25.5 to 27.5°N, tab. 4.4, all significant: $p < .02$). Contrary to that, there is a small, negative correlation between the UI_{SST} and the EA in the higher latitudes (33.5 and 34.5°N, only significant at 34.5°N: $p < .03$).
For the UI_{ERA5}, the NAO shows the highest correlations (> 0.74) at all latitudes with the maximum values occurring in the higher latitudes (< 31.5°N, all significant: $p < .00004$), whereas the EA only shows a low positive and negative correlations for all latitudes (see fig. A.4, not significant).

Latitude (°N)	**Pearsons Correlation**					
	NAO-UI_{SST}	EA-UI_{SST}	NAO-UI_{ERA5}	EA-UI_{ERA5}	NAO-ILD	EA-ILD
25.5	0.627	0.010	0.744	0.184	0.550	-0.240
26.5	0.568	-0.015	0.758	0.179	0.644	-0.308
27.5	0.571	0.010	0.779	0.176	0.593	-0.346
28.5	0.515	0.003	0.771	0.173	0.479	-0.170
29.5	0.489	-0.046	0.709	0.163	0.526	-0.304
30.5	0.493	-0.053	0.675	0.142	0.491	-0.317
31.5	0.483	-0.206	0.807	0.029	0.318	-0.648
32.5	0.523	-0.206	0.864	-0.048	0.243	-0.368
33.5	0.512	-0.338	0.873	-0.086	0.094	-0.662
34.5	0.474	-0.428	0.836	-0.115	0.026	-0.518

Table 4.4: Pearsons correlation coefficient of the Climate Pattern and the UI's/ILD. Pearson's r (rounded) of the winter averages (December to March) for each latitude of the study area and the coastal isothermal layer depth.

In addition to the winter means, the whole time series of the NAO was tested for correlations, however, almost no significant correlation was found with the UI's (except with UI_{SST} at 34.5°N: $p < .03$ and UI_{ERA5} at 34.5°N: $p < .018$). The same applies for the correlation of the UI_{SST} and the EA. Despite a low correlation coefficient between the UI_{ERA5} and the EA, all correlations

are significant ($p < .01$, except at 34.5°N).

When considering the correlation between the ILD at the coast and the climate patterns, a moderate but significant correlation has been detected between the ILD and the NAO at the lower latitudes (0.5 to 0.64, $p < .04$, 25.5-30.5°N) and a moderate, negative correlation between the ILD and the EA at the higher latitudes (-0.52 to -0.66, $p < .04$, 31.5 and >33.5°N, tab. 4.4).

For the offshore area, the NAO shows a moderate, negative correlation above 31.5°N ($p < .004$) with the ILD. The correlation of the winter means of the ILD and the EA as well as all correlations using the summer means of the offshore ILD and the climate pattern reveal no significant correlation (not shown).

Besides correlating the time series, the mean ILD for all positive, negative and neutral events of the NAO and the coupled phase with the EA has been calculated (tab. 4.3). For the winter means (DJFM), the results show a deeper ILD at the coast in years of a NAO+ (104.25 m) and NAO+EA- (116.67 m). Towards the offshore area, the ILD gets shallower in both cases whereas the slope increases during the coupled phase of NAO+EA- (tab. 4.3, fig. 4.10). The signal reverses with NAO- and NAO-EA+ years showing a shallower ILD at the coast and a deepening

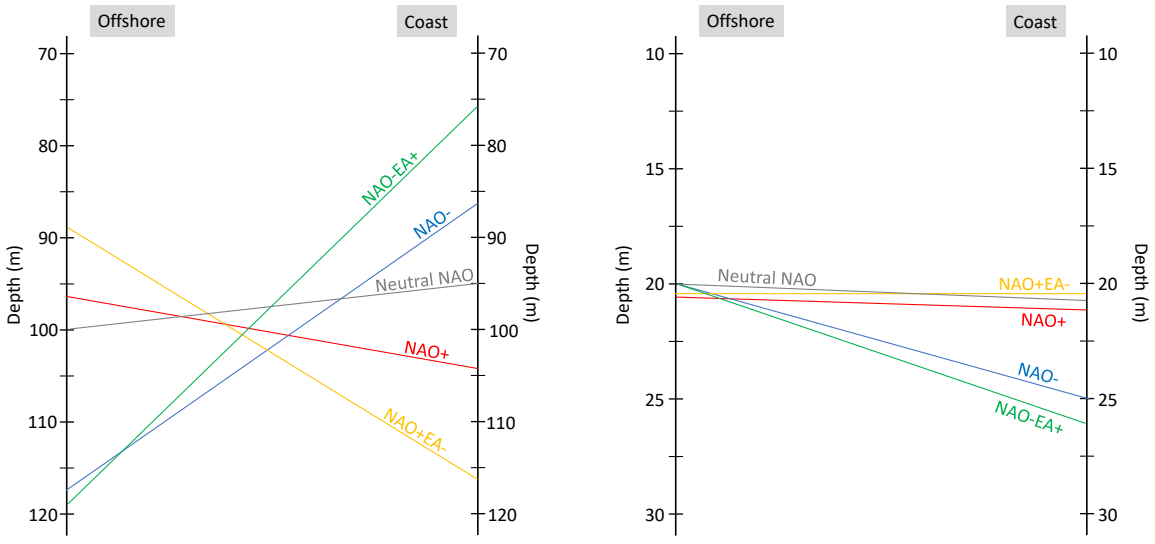

(a) Winter Means **(b)** Summer Means

Figure 4.10: ILD during different phases of the Climate Patterns. Schematic representation of the ILD during positive and negative phases of the NAO as well as its coupled phases with the EA and the ILD in neutral NAO years.

in the offshore area. Again, the slope during coupled phases (NAO-EA+) is greater than in sole NAO- years. The differences of the ILD during the summer month is only visible at the coast where the ILD deepens during NAO- and NAO-EA+ years while it is almost at the same depth for NAO+, NAO+EA- and neutral NAO years (tab. 4.3, fig. 4.10).

5 Discussion

In this section, the results of the three main topics of the study, Upwelling Indices, the upper ocean structure and Climate Pattern, will be analyzed in the context of recent studies. Finally, the impact of climate on the upper ocean structure will be assessed.

5.1 Upwelling Indices

5.1.1 Critical Assessment of the Indices and their Trend

For the calculation of upwelling, three widely used approaches have been selected to obtain indices (UI_{SST}: i.e. Benazzouz et al. 2014, McGregor et al. 2007, Nykjær and Van Camp 1994, Polonsky and Serebrennikov 2018, UI_{ERA5}: i.e. Bakun and Nelson 1991, Cropper et al. 2014, Narayan et al. 2010, Ramos et al. 2013, UI_{PFEL}: i.e. Barton et al. 2013, Cropper et al. 2014, Norton et al. 2002). The results fit well into the existing studies with the main tendency of mostly positive values indicating upwelling between 25 and 35°N. Still, the magnitude of the results differ with the calculation method (see fig. 4.2). Using the normalized data, the UI_{SST} shows the highest index values at 26.5°N and, in comparison to the UI_W indices, higher values in the latitudes above. Therefore, the calculation of the UI_{SST} gives more intense upwelling events in its spatial distribution with the same applying to the temporal scale. Even though the wind variables ($\vec{u}$, $\vec{v}$, τ_x, τ_y) in order to obtain the Ekman transport (Q_x and Q_y) are used in both methods for the UI_W (UI_{ERA5} and UI_{PFEL}), the distribution of events varies with latitudes (see fig. 4.1 and 4.2a). These results can be ascribed to both, the usage of different data sets and different approaches in calculating each index. The latter also becomes apparent in the results of the vertical composites obtained for the UI_{SST}. For upwelling, a clear tendency of cooler water at the coast and warmer water offshore is visible which supports the calculation of the UI_{SST} in general (Benazzouz et al. 2014, Cropper et al. 2014, Pelegrí and Benazzouz 2015, Polonsky and Serebrennikov 2018, Santos et al. 2011, Tamim et al. 2019, ch. 2.4). Still, differences in the surface temperatures along the longitudes and with the different indices (UI_{SST} and UI_{ERA5}) reveal that the highest surface temperatures (25.5-27°C) of the UI_{SST} can be observed offshore below -30°W (approx. 1500 km offshore) whereas the UI_{ERA5} shows the same values below

-40°W (approx. 2500 km offshore). As all composites show a sum of in-situ and modeled potential temperatures for all events exceeding the defined threshold for both UI's, these differences along the same latitudes and a wide continental shelf underlines the importance of choosing an adequate reference location ($SST_{inshore}$ and $SST_{offshore}$) and a suitable temperature threshold in order to obtain the UI_{SST}. The results for the latter UI would have been different if only a point at a distance of 500 km off the coast would have been considered as done in studies by Cropper et al. (2014), Marcello et al. (2011) and others (ch. 2.4) along with a threshold of 5°C to detect upwelling. In the current study, the offshore temperature has been calculated building the mean of the whole offshore area with a variable boundary and all grid values up to -40°W (see tab. 3.2 and red lines in fig. 3.1). As a result, upwelling was detected using the temperatures starting at only 450 km (4.5°) off the coast. It could, however, be a reason why no upwelling with the given threshold was shown at 25.5°N where the distance between $SST_{inshore}$ and $SST_{offshore}$ is smaller. Overall, the results of the current study are in accordance with Narayan et al. (2010) and underline the issue of upwelling indices being very dependent on the used data sets and processing methods. They show the importance of studying upwelling and adapting the calculation of indices in order to make adequate predictions of their variability in the future. Nykjær and Van Camp (1994) and Bessa et al. (2018) already suggested the inclusion of the vertical components, advection and mixing processes especially for all UI's using the Ekman transport as the theory considers a wind-driven ocean circulation in an infinite open ocean (Ekman 1905) which makes the calculation of the transport in the proximity of coasts and capes less accurate. This approach will be addressed further in this study (ch. 5.2 and 5.3.2).

In regards to the controversy of in- or decreasing intensity of upwelling events, no trend has been detected in neither of the UI's during the selected time frame of 25 years (see ch. 2.1). Only the UI_{PFEL} supports the hypothesis of an increase in upwelling intensity (Bakun 1990), however, equal to all other trends, the tendency in either direction is small (slope of -0.2 and 0.1). These results rather indicate a stable coastal upwelling in the CCUS during the past decades. Studies leading to the controversy are done for time spans of 30-60 years, hence, differing results can also be due to the temporal scale which includes both, the total time span and the selected years for the study. Additionally, the usage of different data sets and defined study areas makes a

comparison less robust.

5.1.2 Occurrence of Upwelling in the Study Area

Using the SST data of GREP (in-situ and reanalysis) to calculate the UI_{SST}, upwelling was detected in 29 different month up to 32.5°N. Above this latitude, there is a shift towards reoccurring downwelling events (6 month, tab. 4.1). As the time series plot of the UI_{ERA5} and UI_{PFEL} reveal the same tendency, a transition towards weaker upwelling events can be determined at 33.5°N (fig. 4.2a) which is, again, supported by the occurrence of a few downwelling events being restricted to these upper latitudes (tab. 4.1). By analyzing the monthly climatologies for all, the whole study area as well as below and above 32.5°N, the different distribution and strength of the results with the latitudes become apparent. The wind based UI's clearly show lowest values in the winter months (October to March) which is consistent throughout the latitudes, even though, the annual amplitude decreases with increasing latitude (fig. 5.1). For the UI_{SST}, the lowest index values occur in March and April (25.5-32.5°N) or, in the higher latitudes, in May and June (fig. 5.1c). This time lag between the UI based on wind (UI_{ERA5} and UI_{PFEL}) and UI_{SST} has already been found by Nykjær and Van Camp (1994) and they ascribed it to a possible influence of the bottom topography whereas Benazzouz et al. (2014) listed differences in the inertia of atmosphere and ocean or advection processes as possible causes. A time lag

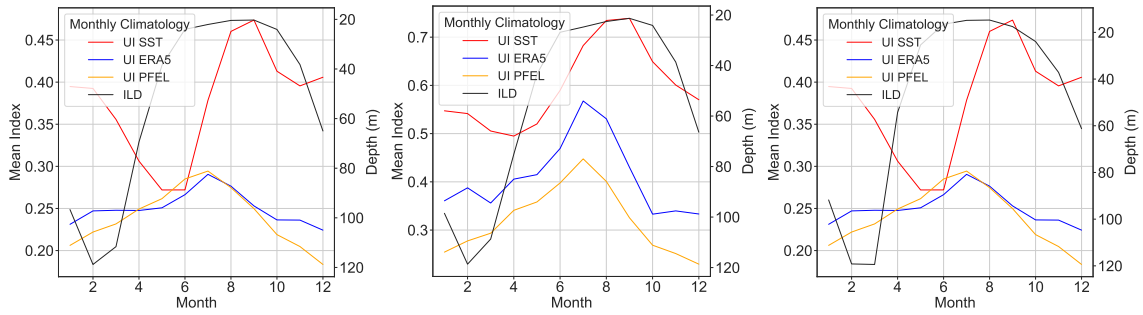

(a) Whole Study Area **(b)** 25.5-32.5°N **(c)** 33.5-34.5°N

Figure 5.1: Monthly climatologies of the Upwelling Indices and the ILD. Climatology of the ILD and the normalized data of the UI's for all latitudes of the study area (a) and divided by latitudes: lower latitudes (b) and the upper latitudes (c), boundary: 32.5°N (plots created in Python, data obtained from NOAA Fisheries 2019 (PFEL), E.U. Copernicus Marine Service Information 2020, and ECMWF Copernicus 2019).

of generally 0-2 months was also observed by other studies (Cropper et al. 2014, Fiúza et al. 1982), however, in the current study a greater lag of 4-5 months has been determined in the upper latitudes. These results suggest an adaptation of the zone of (weak) permanent upwelling (see i.e. Barton et al. 2013, Cropper et al. 2014, Nykjær and Van Camp 1994, fig. 2.1) only up to Cape Beddouza (32.5°N) as already done by Arístegui et al. (2009), Cropper et al. (2014), and Nykjær and Van Camp (1994, adaptation of fig. 2.1). This is also supported by the variation of the ILD which remains deeper in February and March in the upper latitudes (fig. 5.1c). The main causes of this shift are related to less defined coastal winds around 32°N in September as found by Kirk and Speth (1985) and the shift from a wider to a more narrow continental shelf at 33°N (Arístegui et al. 2009) along with a shift in the coastline geometry at Cape Beddouza.
Another striking result found in this study are the strong upwelling index values between 26.5°N and 28.5°N for August and September (tab. 4.1 and A.2). Even though the two strongest upwelling index values were calculated at 32.5°N (Sep. 1994: 6.23°C, Aug. 2012: 6.13°C), the highest values in 16 out of the 29 months occur at 27.5°N. Nykjær and Van Camp (1994) revealed the same findings and Bessa et al. (2020) were able to identify Cape Bojador (26.5°N) as a source of upwelling in the region.

5.2 Ocean Stratification

The composite maps of the up- and downwelling events give a good insight into the vertical structure of the upper ocean. The cooler temperatures along the continental shelf during upwelling events and the gradient of the isotherms towards the surface clearly indicate the vertical flux of subsurface water onto the surface in order to replace the offshore flow of surface water due to Ekman transport off the coast and Ekman suction. Consequently, the potential temperatures offshore are generally warmer.
The vertical profiles of upwelling events (fig. 4.5) show the same distribution. Along the surface of the nearshore area, the potential temperature is cooler compared to the offshore area and the density higher. With depth, the stratification increases and the differences of temperature and density between the near- and offshore area decreases, however, the nearshore values are always smaller than the mean offshore values. The ILD of the months with upwelling is deeper than the

one detected for years without upwelling. For the UI_{SST}, the changes in the ILD are less distinct (deepening by 1 m at the coast and 2.5 m offshore), however, for the UI_{ERA5}, the ILD deepens by almost 5 m during upwelling events (tab. 4.2).

Contrary to the upwelling composites, the ones plotted for downwelling differ with the selected UI. The isotherms are more parallel to the surface in both but the upper layer of the UI_{ERA5} downwelling events reveals a deeper isothermal layer (fig. 4.4b). With depth, both composites reveal a less rapid change in the potential temperature offshore, however, the isotherms are still more parallel in the UI_{ERA5} composite. Both composites for downwelling events reveal the signature of the process with relatively warmer potential temperatures at the coast. This indicates the downward movement of warmer surface waters due to Ekman pumping. The vertical profiles confirm the findings of the composite maps with the nearshore temperature (density) profiles being slighty cooler (denser) than the mean offshore values but still not cooler (denser) than the computed minimum (maximum) values (fig. 4.6a and 4.6b). The same applies for the UI_{ERA5} profiles (fig. 4.6c and 4.6d), with the difference being the deeper isothermal layer depth.

While downwelling was detected in June of different years using the UI_{SST} and the ones for UI_{ERA5} are in January and December 1996, the difference of the vertical structure for these events is due to their different timings rather than the usage of different UI's (see ch. 5.1). In general, the ILD is more shallow in years of downwelling events compared to the years where the UI's are neutral (tab. 4.2) which is also confirmed by the significant correlation detected for the ILD and the UI's. Despite these changes with up- and downwelling, there is a clear annual cycle in the time series of the computed ILD values (fig. 4.7) which has already been subject to earlier studies (ch. 2.3). While Troupin et al. (2010) found an ILD up to 150 m in February, the current study shows the deepest ILD of 199.79 to 244.89 m in March. The results indicate pronounced surface mixing during winter where the winds are strongest and heat is lost into the atmosphere. In summer, high stratification can be observed as a result of weak winds and surface warming through solar radiation (Barton et al. 2013). Still, Bessa et al. (2019 and 2020) found cooler surface temperatures when the ILD is shallower and were able to correlate this to the upwelling intensity. The significant correlation found in this study supports the latter. Nevertheless, a deepening of the ILD was found with increased upwelling intensity which suggests a

deeper ILD with cooler SSTs (tab. 4.2). Even though the SSTs are influenced through upwelling, for the analyzed vertical structure of these events the drivers for the ILD on an annual scale are rather the prevailing wind conditions as well as buoyancy forcings and heat fluxes (Boyer et al. 2013, Chavez and Messié 2009, Narayan et al. 2010, Somavilla et al. 2017). Therefore, using solely the ILD to determine upwelling can lead to faulty results as the direction of the wind and the resulting Ekman transport plays a major role (Benazzouz et al. 2014, Polonsky and Serebrennikov 2018). The results of the current study indicate this, however, further research taking the wind into account is necessary.

In order to consider the impact of the Canary Islands, the vertical composite map at 28.5°N (9 months) was built (fig. A.5). It does, however, not show any effects on the vertical structure of the upper ocean during upwelling events when comparing it to the composites for 26.5 and 30.5°N (fig. 4.3a and 4.3b). Knoll et al. (2002) found a southward flow in the channel between the Canary Islands and the African mainland which is similar to the Canary Current, however, they did not find an intensification with the summer trade winds. Still, this flow can induce Ekman Transport off the coast and, hence, upwelling. Another factor leading to similar results despite the islands can be related to the used data set (GREP from CMEMS) which consists of both, in-situ and modeled data. It is not known how islands and the continental shelf affects the model. The same applies for the Capes along the coast. As the local topography does have an impact on upwelling (ch. 5.1), a response in the vertical structure is likely but it is not possible to draw any conclusion using the results of the current study. Future research is necessary to investigate this further and to elaborate existing studies (Bessa et al. 2019 and 2020).

5.3 The Impact of the Climate Indices

The influence of the climate patterns will be assessed in two aspects. Firstly, their impact on the detected up- and downwelling events will be analyzed and, secondly, on the upper ocean structure which is mainly done using the ILD and the vertical distribution of the potential temperature.

5.3.1 Climate and Upwelling

The NAO is related to the Azores High Pressure System and, therefore, the wind in the North Atlantic region (Hurrell and Van Loon 1997, Neves et al. 2019, Yamamoto et al. 2020, Yan et al. 2004). Since the wind is also the driver for the upwelling intensity in the Canary Current (Nykjær and Van Camp 1994, Wooster et al. 1976), it was expected to see correlations between both, the climate patterns and upwelling. The Pearson's correlation coefficient calculated in this study supports the hypothesis showing a high, significant correlation between the winter means of both, the NAO and the UI_{ERA5}, and a moderate to high correlation with the winter means of the UI_{SST} (see tab. 4.4) which get even better when correlating the NAO with a time-lagged UI_{SST} (tab. 5.1). Considering the summer month where most of the upwelling occurs, the correlation gets weaker (low degree, not shown). These findings are not surprising as the NAO is known to have a weak signal in the summer months (Pardo et al. 2011) and they confirm the results of Narayan et al. (2010) who only found ambiguous correlations between the NAO and the UI_{SST}. Additionally, the authors found a negative correlation with the wind stress along the NW African coast which is not represented in neither of the correlations (winter means, summer means) of the NAO and the UI_{ERA5} in this study. The steady decrease of the correlation with the UI_{ERA5} data with increasing latitudes also coincides with the findings of Pardo et al. (2011) who found strongest correlations between the NAO and the UI based on wind in Portugal with a decrease until 20°N. The authors also found the EA to play a stronger role below this latitude whereas the increasing correlation found with increasing latitude in the study area as well as the main spatial pattern of the EA suggest the opposite.

In order to analyze the impact of the NAO and the EA on the upwelling further, the total month of their different phases as well as for up- and downwelling have been counted for each year. During the time span of the study, 12 years of positive NAO events have been detected and upwelling occurred in nine of them (75%) with a total number of 16 months out of 29 months (55%, UI_{SST}). Despite the occurrence in the same years, the intensity of the NAO index does not affect the intensity and occurrence of the upwelling throughout the year. Upwelling was observed in three months in 1999 (July to September), a year with a low NAO+ value (0.54), and in only one to two months of events with higher index values. The high NAO values in

the beginning of the 1990s do not coincide with a higher intensity or occurrence of upwelling events. Additionally, in 5 years (13 months) with a neutral NAO state, upwelling occurred in one to three months. The same can be observed for NAO- and downwelling. In one out of six events, downwelling coincides with a clear negative phase, the other five events occur during neutral phases. The events can also not be explained with a lag or a persistent NAO for a few winters (Visbeck et al. 2003, see tab. A.2).

Taking the phase of the EA into consideration, the occurrence of three consecutive month with upwelling in 1999 can be explained as the EA is in a negative phase (-0.81, NAO+EA-). The second NAO+EA- year, 2012 (NAO: 1.35, EA: -1), also shows two month of upwelling. In both years, the events start occurring in July whereas in years of positive NAO they occur mostly between August and September, and in some cases up to November of the same year. Still, in years of neutral NAO upwelling was detected for July to November, too. The phase and strength of the EA+ does not seem to impact these events in a clear pattern: in years with high index values, the occurrence of upwelling varies between one and three months. Again, the same can be observed for detected downwelling events.

The same pattern applies for the UI_{ERA5} (not shown). Upwelling occurs during NAO+ (17 out

Latitude (°N)	**Pearsons Correlation**		
	NAO-SST (DJFM)	NAO-SST (JFMA)	NAO-ERA5
25.5	0.627	0.607	0.744
26.5	0.568	0.520	0.758
27.5	0.571	0.542	0.779
28.5	0.515	0.553	0.771
29.5	0.489	0.535	0.709
30.5	0.493	0.551	0.675
31.5	0.483	0.568	0.807
32.5	0.523	0.621	0.864
33.5	0.512	0.610	0.873
34.5	0.474	0.586	0.836

Table 5.1: Pearsons correlation coefficient of the NAO and the time-lagged UI_{SST}. Pearson's r (rounded) of the winter averages (December to March) of the NAO and the SST (December to March and January to April) for each latitude of the study area, correlation with the ERA5 data as comparison.

of 38 month) and even during NAO- events (3 out of 38 month). During the remaining 18 month of detected upwelling, the NAO is in a neutral phase. Only during downwelling, both detected month coincide with NAO-.

Despite these ambiguous results, the composite maps build for the different phases of the NAO clearly show the signature of upwelling during NAO+. The potential temperatures are cooler along the coastline than in the offshore area and this pattern is visible throughout the depth (fig. 4.9). Even though the potential temperature along the coast is also cooler during NAO- years, the difference is smaller. These results show that the NAO and the EA do have an impact on the wind, SST and upwelling, however, it can not be identified as a main driver for upwelling processes in the Canary Current Upwelling System.

5.3.2 Climate and the Upper Ocean Structure

The shift of the westerly winds with the prevailing phase of the NAO is a well-studied phenomenon and represented in the composite maps (ch. 2.5). In the upper ocean, the southward shift of these winds become apparent during both NAO- and NAO-EA+ events (Angell and Korshover 1974, Limpasuvan and Hartmann 2000, Lorenz and Hartmann 2003, Luo et al. 2007, Serreze et al. 1997, Yamaguchi and Suga 2019). At the surface, the isotherms are almost parallel from west to east with changes in the proximity of the coastline. During NAO+ and NAO+EA-, the southwest-northeast gradient of the surface layer indicates a different forcing.

The differences of the ILD based on the prevailing phase of the patterns become apparent with depth. For the NAO- and NAO-EA+, the transition of the isothermal layer and the deep ocean water is between composites of the 47.21 and 97.04 m depth at the coast, whereas the ILD in the offshore area is deeper than 97.04 m. This transition explains the disappearance of the north to south temperature gradient at the coast and a continuation of the sea-air-interaction offshore where the north-south gradient is maintained. Contrary to that and regardless of the ILD, no SST anomalies as found by Delworth and Zeng (2016) and Yamaguchi and Suga (2019) can be observed in the offshore area during NAO+ years. This should, however, be more dominant in the northern areas of the Atlantic Ocean and can become visible with changes in the ocean dynamics and circulation with a time lag of several years to decades (Visbeck et al. 2003). Along

the coast, cooler potential temperatures can be observed as a result of enhanced trade winds between 10 and 30°N in NAO+ years (fig. 4.9, Visbeck et al. 2003) which coincides with the signal of upwelling (fig. 4.3a, 4.3b and 4.4a, fig. 5.2).

Hurrell (1995) investigated the wind conditions over the North Atlantic and its influence on the moist transport during positive and negative NAO events. The results at the surface of the composite maps coincide with his findings. Beside the southerly shift and weakening of the westerlies and moist transport during NAO-, which also affect the study area especially in the northern parts, he found a shift of winds towards the southwest in the southwestern part of the study area during NAO+. These patterns explain the spatial distribution found at the surface and throughout the depths of the composite maps.

The significant correlation between the climate patterns and the ILD confirm their signal with depth. The winter (summer) NAO- signal of a shallow (deep) ILD near- and a deep (shallow) one offshore coincides with studies of the global ILD (Kara 2003). Still, changes in the ILD with NAO+ and NAO- in comparison to neutral NAO years indicate anomalies and a relationship between the climate index and the ILD (tab. 4.3 and fig. 4.10). The deepening of the winter ILD during NAO- phases in the offshore area supports the influence in relation to the shift of the westerly winds enhancing the atmosphere-ocean-interaction and a heat loss of the ocean. In NAO+ years with a strengthening of the winds, Delworth et al. (2017) and Delworth and Zeng (2016) found an enhanced heat flux from the ocean into the atmosphere leading to an increase in density and a deepening of the ILD. The same has been observed at the coast during the winter month (fig. 4.10), however, the results of this study reveal a shallower ILD offshore during NAO+ events. This can be due to the location of the westerlies farther north during the NAO+ phases and, therefore, to reduced mixing of the upper ocean (Häkkinen 1999, Limpasuvan and Hartmann 2000, Lorenz and Hartmann 2003, Luo et al. 2007, Serreze et al. 1997, Visbeck et al. 2003). Additionally, other forcings to the temperature like buoyancy forces might play a role (heat and salt exchange, Somavilla et al. 2017).

This study shows a variation of the upper ocean depending on the prevailing climate. Different phases of the NAO coincide with changes in the potential temperature and the ILD which is represented in existing correlations. Still, the main forcing causing changes in the upper ocean

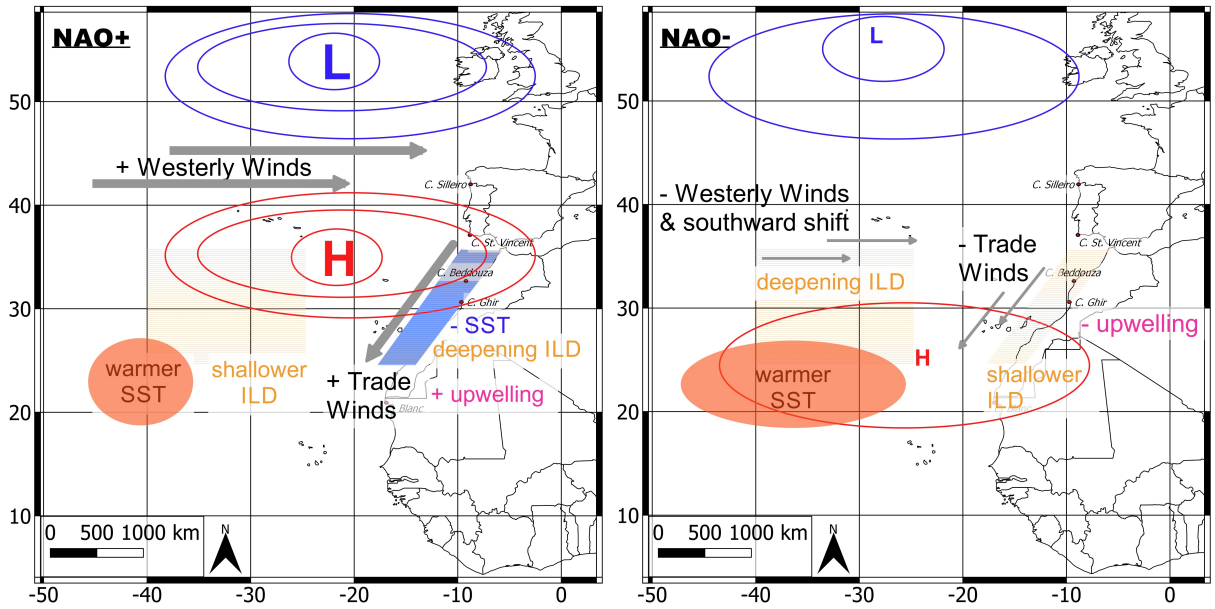

(a) NAO+ **(b)** NAO-

Figure 5.2: Impact of the NAO on the atmospheric and oceanic conditions. Variations of the Azores High and the Icelandic Low Pressure Systems during NAO+ (a) and NAO- (b) with the resulting changes in the winds, upwelling and the ILD in the study area (schematic).

structure cannot be ascribed solely to the climate patterns and will need to be investigated further in future studies. Rodwell et al. (1999) suggest a relationship between SST and the NAO with SST anomalies being able to force a NAO-like pattern in the atmosphere. Additionally, the cause and effect relationship between the AMOC, the thermohaline circulation and the NAO needs to be taken into account as well as the related changes in the upper ocean structure (Delworth and Dixon 2000, Delworth and Zeng 2016, Delworth et al. 2017, Hurrell et al. 2001). All of these studies suggest impacts of the ocean heat flux and ocean dynamics as an important factor. Besides these local forcings affecting the thermocline and the stratification, Bonino et al. (2019) found that the upwelling in the CCUS can be explained to a high percentage by remote forcings such as coastal trapped waves and they added the greenhouse gases as another possible impact on the upwelling intensity. For the California and the Benguela Current, the investigation of remote forcings using models revealed a similar trend. Basin scale climate variability and Kelvin waves were found to have a greater impact on an interannual scale and beneath the surface of the ocean. Opposed to that, local forcings (wind stress, surface heat flux) were found to play a role on a smaller time scale (around 100 days) and mainly on the surface (Bachèlery et al. 2016,

Frischknecht et al. 2015, Jacox et al. 2015, Polo et al. 2008). These studies show that there are many possible forcings and interactions in the ocean which are not fully understood yet and need further research. Considering all the parameters and observed time lags of several years to decades, further studies using complex models can be helpful which is confirmed by all recent studies about the ocean dynamics and different forcings.

5.4 Limitations of the Study

One of the main issues in the research of the upper ocean is the lack of available in-situ observations (Bessa et al. 2019, de Boyer Montégut et al. 2007, Hu et al. 2019, Kara 2003, Levitus 2005, Levitus et al. 2000, Moon and Song 2014, Visbeck et al. 2003). One of the aims of the current study was the usage of WOA18 data, however, the sparse data made it not possible to calculated up- and downwelling events and create a continuous time series of these events (fig. 3.1). The usage of the GREP data allowed to analyze the objectives set for this study, still, it needs to be considered that this data is already averaged and interpolated. All results may, therefore, deviate from the in-situ ocean structure.

6 Conclusion

The focus of this study is to assess the impact of climate on the upper ocean structure in a part of the Canary Current Upwelling System. For the selected study area between 25 and 35°N, upwelling indices have been calculated and the vertical structure of these events analyzed. Additionally, the results of both parts have been correlated with the NAO and the EA index.

The selected study area comprises the central part of the CCUS with weak annual upwelling and an intensification during the summer month which allows the establishment of relationships between upwelling and its possible drivers. Upwelling has been determined calculating indices based on temperature differences (UI_{SST}) and on wind stress with the resulting Ekman transport (UI_{ERA5} and UI_{PFEL}). While all UI's indicate mostly upwelling in the study area, the assessment of the upwelling indices has shown the temporal and spatial variation depending on the index. The results imply that the calculation of the indices needs to be adapted in order to obtain coherent values which requires a full understanding the process of upwelling and ocean dynamics. Still, all indices have revealed strong upwelling events until 32.5°N and downwelling only above which is related to the prevailing winds and the shelf characteristics. Additionally, a lag of four to five months has been found between the UI_W and the UI_{SST} which becomes more apparent above 32.5°N.

Using two different approaches (UI_{SST} and UI_{ERA5}), the study has shown that there are changes in the vertical structure of the upper ocean for up- and downwelling with differences between the near- and the offshore area. While the SSTs are cooler at the coast (20°C) than in the offshore area (25°C), the distinct pattern of upwelling with an offshore Ekman transport and the replacement of the surface water by cooler water at the coast is reflected in the upward gradient of the isotherms towards the coast and a slightly deeper ILD. The gradient of the isotherms reverses during downwelling events in the proximity to the coast and the ILD becomes shallower. In general, the ILD calculated for this study shows an annual cycle with a deepening during the winter month and a more shallow ILD during summer with a higher variability at the coast.

The signal of the NAO varies throughout the year with a strong correlation with the UI's found in the winter months and in the south (UI_{SST}) and north (UI_{ERA5}) of the study area, respectively. The strongest correlation occurs with the UI_{ERA5}. The ILD varies with the prevailing phase of

the climate pattern. During winter, the ILD is deeper (shallower) at the coast (offshore) in positive phases of the NAO and opposed to that during its negative phases which is also represented in the correlation of both, the NAO and the ILD. During years of coupled phases, the variation of the ILD is enhanced with a further deepening at the coast and a more shallow ILD offshore during NAO+EA- years. The same enhancement of an even shallower ILD at the coast and a deeper one offshore is detected during NAO-EA+ years.

During NAO+, the potential temperatures along the coastline reveal the same signal of cooler temperatures as during upwelling events. Still, upwelling events with different intensities also seem to occur independent from the NAO and the ILD varies annually with different forcings. It is not possible to find a cause and effect relationship solely between both, the NAO and the ILD. Upwelling as well as the vertical structure is rather forced by complex ocean dynamics such as buoyancy, currents, and heat exchange. The study suggests that a more holistic approach is needed to investigate upwelling which can also help in the existing controversy of the changes in the occurrence and strength of the events in regards to climate change.

The study also shows the importance of marine research programs in order to understand the dynamics. The lack of in-situ data is a major issue in this field which cannot completely be replaced by models. For future research, it is also important to investigate the impact of the increasing greenhouse gases further (Bakun 1990, Bonino et al. 2019).

References

Angell, J. K. and Korshover, J. (1974). Quasi-biennial and long-term fluctuations in the centres of action, *Monthly Weather Review* **102**: 669–678.

Arístegui, J., Barton, E. D., Álvarez Salgado, X. A., Santos, A. M. P., Figueiras, F. G., Kifani, S., Hernández-León, S., Mason, E., Machú, E. and Demarcq, H. (2009). Sub-regional ecosystem variability in the Canary Current upwelling, *Progress in Oceanography* **83**(1-4): 33–48.

Bachèlery, M., Illig, S. and Dadou, I. (2016). Interannual variability in the south-e ast a tlantic ocean, focusing on the benguela upwelling system: Remote versus local forcing, *Journal of Geophysical Research: Oceans* **121**(1): 284–310.

Bakun, A. (1973). Coastal upwelling indices, west coast of North America, *NOAA Technical Report NMFS SSRF-671*, US Department of Commerce.

Bakun, A. (1975). Daily and Weekly Upwelling Indices, West Coast of North America 1967-73, *NOAA technical report NMFS SSRF* **16**: 124.

Bakun, A. (1990). Global Climate Change and Intensification of Coastal Ocean Upwelling, *Science* **247**(4939): 198–201.

Bakun, A. and Nelson, C. S. (1991). The Seasonal Cycle of Wind-Stress Curl in Subtropical Eastern Boundary Current Regions, *Journal of Physical Oceanography* **21**: 1815–1834.

Balaguru, K., Foltz, G. R., Leung, L. R. and Emanuel, K. A. (2016). Global warming-induced upper-ocean freshening and the intensification of super typhoons, *Nature Communications* **7**(1): 13670.

Barnston, A. G. and Livezey, R. E. (1987). Classification, seasonality and persistence of low-frequency atmospheric circulation patterns, *Monthly Weather Review* **115**: 1083–1126.

Barton, E., Arístegui, J., Tett, P., Cantón, M., Garcıa-Braun, J., Hernández-León, S., Nykjaer, L., Almeida, C., Almunia, J., Ballesteros, S., Basterretxea, G., Escánez, J., Garcıa-Weill, L., Hernández-Guerra, A., López-Laatzen, F., Molina, R., Montero, M., Navarro-Pérez, E.,

Rodrıguez, J., van Lenning, K., Vélez, H. and Wild, K. (1998). The transition zone of the Canary Current upwelling region, *Progress in Oceanography* **41**(4): 455–504.

Barton, E., Field, D. and Roy, C. (2013). Canary current upwelling: More or less?, *Progress in Oceanography* **116**: 167–178.

Bastos, A., Janssens, I. A., Gouveia, C. M., Trigo, R. M., Ciais, P., Chevallier, F., Peñuelas, J., Rödenbeck, C., Piao, S., Friedlingstein, P. and Running, S. W. (2016). European land CO2 sink influenced by NAO and East-Atlantic Pattern coupling, *Nature Communications* **7**(1): 1–9.

Benazzouz, A., Mordane, S., Orbi, A., Chagdali, M., Hilmi, K., Atillah, A., Lluís Pelegrí, J. and Hervé, D. (2014). An improved coastal upwelling index from sea surface temperature using satellite-based approach – The case of the Canary Current upwelling system, *Continental Shelf Research* **81**: 38–54.

Benesty, J., Chen, J. and Cohen, I. (2009). Pearson Correlation Coefficient, *Noise Reduction in Speech Processing*, Vol. 2 of *Springer Topics in Signal Processing*, Springer, Heidelberg, pp. 37–40.

Bernard, B., Madec, G., Penduff, T., Molines, J.-M., Treguier, A.-M., Le Sommer, J., Beckmann, A., Biastoch, A., Böning, C., Dengg, J., Derval, C., Durand, E., Gulev, S., Remy, E., Talandier, C., Theetten, S., Maltrud, M., McClean, J. and De Cuevas, B. (2006). Impact of partial steps and momentum advection schemes in a global ocean circulation model at eddy-permitting resolution, *Ocean Dynamics* **56**(5-6): 543–567.

Bessa, I., Makaoui, A., Agouzouk, A., Hilmi, K., Idrissi, M., Ettahiri, O. and Afifi, M. (2017). Seasonal Variability of the Ocean Mixed Layer Depth in Moroccan Upwelling Areas derived from in situ Profiles, *International Journal of Advanced Research* **5**(3): 1754–1762.

Bessa, I., Makaoui, A., Agouzouk, A., Idrissi, M., Hilmi, K. and Afifi, M. (2019). Seasonal variability of the ocean mixed layer depth depending on the cape Ghir filament and the upwelling in the Moroccan Atlantic coast, *Materials Today: Proceedings* **13**: 637–645.

Bessa, I., Makaoui, A., Agouzouk, A., Idrissi, M., Hilmi, K. and Afifi, M. (2020). Variability of the ocean mixed layer depth and the upwelling activity in the Cape Bojador, Morocco, *Modeling Earth Systems and Environment* **6**(3): 1345–1355.

Bessa, I., Makaoui, A., Hilmi, K. and Afifi, M. (2018). Variability of the mixed layer depth and the ocean surface properties in the Cape Ghir region, Morocco for the period 2002–2014, *Modeling Earth Systems and Environment* **4**(1): 151–160.

Blockley, E. W., Martin, M. J., McLaren, A. J., Ryan, A. G., Waters, J., Lea, D. J., Mirouze, I., Peterson, K. A., Sellar, A. and Storkey, D. (2014). Recent development of the Met Office operational ocean forecasting system: an overview and assessment of the new Global FOAM forecasts, *Geoscientific Model Development* **7**(6): 2613–2638.

Bonino, G., Di Lorenzo, E., Masina, S. and Iovino, D. (2019). Interannual to decadal variability within and across the major Eastern Boundary Upwelling Systems, *Scientific Reports* **9**(19949): 1–14.

Boyer, T. P., Antonov, J. I., Baranova, O. K., Coleman, C., Garcia, H. E., Grodsky, A., Johnson, D. R., Locarnini, R. A., Mishonov, A. V., O'Brien, T. D., Paver, C. R., Reagan, J. R., Seidov, D., Smolyar, I. V. and Zweng, M. M. (2013). World Ocean Database 2013, NOAA Atlas NESDIS 72.

Bueh, C. and Nakamura, H. (2007). Scandinavian pattern and its climatic impact, *Quarterly Journal of the Royal Meteorological Society* **133**(629): 2117–2131.

Carr, M.-E. and Kearns, E. J. (2003). Production regimes in four Eastern Boundary Current systems, *Deep Sea Research Part II* **50**(2003): 3199–3221.

Chavez, F. P. and Messié, M. (2009). A comparison of Eastern Boundary Upwelling Ecosystems, *Progress in Oceanography* **83**(1-4): 80–96.

Chu, P. C. and Fan, C. (2010). Optimal Linear Fitting for Objective Determination of Ocean Mixed Layer Depth from Glider Profiles, *Journal of Atmospheric and Oceanic Technology* **27**(11): 1893–1898.

Chu, P. C. and Fan, C. (2011). Determination of Ocean Mixed Layer Depth from Profile Data, *Integrated Observing and Assimilation Systems for the Atmosphere, Oceans and Land Surface (IOAS-AOLS)*, American Meterological Society, Seattle, pp. 1001–1008.

Comas-Bru, L. and Hernández, A. (2018). Reconciling North Atlantic climate modes: revised monthly indices for the East Atlantic and the Scandinavian patterns beyond the 20th century, *Earth System Science Data* **10**: 2329–2344.

Copernicus Monitoring Environment Marine Service (2020). Global Ocean Ensemble Physics Reanalysis (PHY_001_026).
URL: *https://resources.marine.copernicus.eu/?option=com_cswtask=results?option=com_cswview=detailsproduct$_i$d* = *GLOBAL*_001_026

Cropper, T. E., Hanna, E. and Bigg, G. R. (2014). Spatial and temporal seasonal trends in coastal upwelling off Northwest Africa, 1981–2012, *Deep Sea Research Part I* **86**: 94–111.

de Boyer Montégut, C., Mignot, J., Lazar, A. and Cravatte, S. (2007). Control of salinity on the mixed layer depth in the world ocean: 1. General description, *Journal of Geophysical Research* **112**(C6): C06011.

Delworth, T. L. and Dixon, K. W. (2000). Implications of the Recent Trend in the Arctic/North Atlantic Oscillation for the North Atlantic Thermohaline Circulation, *Journal of Climate* **13**: 7.

Delworth, T. L. and Zeng, F. (2016). The Impact of the North Atlantic Oscillation on Climate through Its Influence on the Atlantic Meridional Overturning Circulation, *Journal of Climate* **29**(3): 941–962.

Delworth, T. L., Zeng, F., Zhang, L., Zhang, R., Vecchi, G. A. and Yang, X. (2017). The Central Role of Ocean Dynamics in Connecting the North Atlantic Oscillation to the Extratropical Component of the Atlantic Multidecadal Oscillation, *Journal of Climate* **30**(10): 3789–3805.

Desportes, C., Garric, G., Régnier, C., Drévillon, M., Parent, L., Garric, G., Drillet, Y., Masina, S., Storto, A., Mirouze, I., Cipollone, A., Zuo, H., Balmaseda, M., Peterson,

D., Wood, R., Jackson, L., Mulet, S. and Greiner, E. (2017). Quality Information Document For Global Ocean Reanalysis Multi-model Ensemble Products GREP-V1 GLOBAL-REANALYSIS-PHY-001-026, p. 40.

ECMWF Copernicus (2019). ERA5 monthly averaged data on pressure levels from 1979 to present.
URL: *https://cds.climate.copernicus.eu*

Ekman, W. (1905). On the influence of the Earth's rotation on ocean currents, *Arkiv för Matematik, Astronomi och Fysik* **2**(11): 1–52.

Enfield, D. B. and Mayer, D. A. (1997). Tropical Atlantic sea surface temperature variability and its relation to El Niño-Southern Oscillation, *Journal of Geophysical Research: Oceans* **102**(C1): 929–945.

E.U. Copernicus Marine Service Information (2020). CMEMS FTP-Server.
URL: *ftp://my.cmems-du.eu*

Fiúza, A. F. d. G., de Macedo, M. E. and Guerreiro, M. R. (1982). Climatological space and time variation of the Portuguese coastal upwelling, *Oceanologica Acta* **5**(1): 31–40.

Freudenthal, T., Meggers, H., Henderiks, J., Kuhlmann, H., Moreno, A. and Wefer, G. (2002). Upwelling intensity and filament activity off Morocco during the last 250,000 years, *Deep Sea Research Part II: Topical Studies in Oceanography* **49**(17): 3655–3674.

Frischknecht, M., Münnich, M. and Gruber, N. (2015). Remote versus local influence of ENSO on the California Current System, *Journal of Geophysical Research: Oceans* **120**(2): 1353–1374.

Gajera, V., Shubham, Gupta, R. and Jana, P. K. (2016). An effective Multi-Objective task scheduling algorithm using Min-Max normalization in cloud computing, *2016 2nd International Conference on Applied and Theoretical Computing and Communication Technology (iCATccT)*, IEEE, Bangalore, India, pp. 812–816.

García-Serrano, J., Cassou, C., Douville, H., Giannini, A. and Doblas-Reyes, F. J. (2017). Revisiting the ENSO Teleconnection to the Tropical North Atlantic, *Journal of Climate* **30**(17): 6945–6957.

Gómez-Letona, M., Ramos, A. G., Coca, J. and Arístegui, J. (2017). Trends in Primary Production in the Canary Current Upwelling System—A Regional Perspective Comparing Remote Sensing Models, *Frontiers in Marine Science* **4**: 370.

Gnanaseelan, C., Chowdary, J. S., Mishra, A. K. and Salvekar, P. S. (2003). Interannual Variability of Upper Ocean Heat content in the Northern Indian Ocean, *Journal of Indian Geophysical Union* **7**(4): 193–200.

Gruber, N., Lachkar, Z., Frenzel, H., Marchesiello, P., Münnich, M., McWilliams, J. C., Nagai, T. and Plattner, G.-K. (2011). Eddy-induced reduction of biological production in eastern boundary upwelling systems, *Nature Geoscience* **4**(11): 787–792.

Häkkinen, S. (1999). Variability of the simulated meridional heat transport in the North Atlantic for the period 1951-1993, *Journal of Geophysical Research: Oceans* **104**(C5): 10991–11007.

Hu, S., Zhang, Y., Feng, M., Du, Y., Sprintall, J., Wang, F., Hu, D., Xie, Q. and Chai, F. (2019). Interannual to Decadal Variability of Upper-Ocean Salinity in the Southern Indian Ocean and the Role of the Indonesian Throughflow, *Journal of Climate* **32**(19): 6403–6421.

Hughes, P. and Barton, E. (1974). Stratification and water mass structure in the upwelling area off northwest Africa in April/May 1969, *Deep Sea Research and Oceanographic Abstracts* **21**(8): 611–628.

Hurrell, J. W. (1995). Decadal trends in the North Atlantic Oscillation and relationships to regional temperature and precipitation, *Science* **269**: 676–679.

Hurrell, J. W., Kushnir, Y., Ottersen, G. and Visbeck, M. (2003). An overview of the North Atlantic Oscillation, *in* J. W. Hurrell, Y. Kushnir, G. Ottersen and M. Visbeck (eds), *Geophysical Monograph Series*, Vol. 134, American Geophysical Union, Washington, D. C., pp. 1–35.

Hurrell, J. W., Kushnir, Y. and Visbeck, M. (2001). The North Atlantic Oscillation, *Science* **291**: 603–604.

Hurrell, J. W. and Van Loon, H. (1997). Decadal Variations in Climate Associated with the North Atlantic Oscillation, *Climatic Change* **36**: 301–326.

Iglesias, I., Lorenzo, M. N., Lázaro, C., Fernandes, M. J. and Bastos, L. (2017). Sea level anomaly in the North Atlantic and seas around Europe: Long-term variability and response to North Atlantic teleconnection patterns, *Science of The Total Environment* **609**: 861–874.

IPCC (2019). IPCC Special Report on the Ocean and Cryosphere in a Changing Climate, *Technical report*, In press.

Jacox, M. G., Bograd, S. J., Hazen, E. L. and Fiechter, J. (2015). Sensitivity of the California Current nutrient supply to wind, heat, and remote ocean forcing, *Geophysical Research Letters* **42**(14): 5950–5957.

Kalimeris, A., Ranieri, E., Founda, D. and Norrant, C. (2017). Variability modes of precipitation along a Central Mediterranean area and their relations with ENSO, NAO, and other climatic patterns, *Atmospheric Research* **198**: 56–80.

Kara, A. B. (2003). Mixed layer depth variability over the global ocean, *Journal of Geophysical Research* **108**(C3): 3079.

Kara, A. B., Rochford, P. A. and Hurlburt, H. E. (2000). Mixed layer depth variability and barrier layer formation over the North Pacific Ocean, *Journal of Geophysical Research: Oceans* **105**(C7): 16783–16801.

Kirk, A. and Speth, P. (1985). Wind conditions along the coast of northwest Africa and Portugal during 1972-79, *Tropical Ocean-Atmosphere Newsletter* **30**: 15–16.

Knippertz, P., Christoph, M. and Speth, P. (2003). Long-term precipitation variability in Morocco and the link to the large-scale circulation in recent and future climates, *Meteorology and Atmospheric Physics* **83**(1-2): 67–88.

Knoll, M., Hernández-Guerra, A., Lenz, B., López Laatzen, F., Machın, F., Müller, T. and Siedler, G. (2002). The Eastern Boundary Current system between the Canary Islands and the African Coast, *Deep Sea Research Part II: Topical Studies in Oceanography* **49**(17): 3427–3440.

Large, W. G. and Pond, S. (1981). Open Ocean Momentum Flux Measurements in Moderate to Strong Winds, *Journal of Physical Oceanography* **11**: 324–336.

Lellouche, J.-M., Le Galloudec, O., Drévillon, M., Régnier, C., Greiner, E., Garric, G., Ferry, N., Desportes, C., Testut, C.-E., Bricaud, C., Bourdallé-Badie, R., Tranchant, B., Benkiran, M., Drillet, Y., Daudin, A. and De Nicola, C. (2013). Evaluation of global monitoring and forecasting systems at Mercator Océan, *Ocean Science* **9**(1): 57–81.

Levitus, S. (2005). Warming of the world ocean, 1955–2003, *Geophysical Research Letters* **32**(2): L02604.

Levitus, S., Antonov, J. I., Boyer, T. P. and Stephens, C. (2000). Warming of the World Ocean, *Science* **287**: 5.

Limpasuvan, V. and Hartmann, D. L. (2000). Wave-Maintained Annular Modes of Climate Variability, *Journal of Climate* **13**: 16.

Locarnini, R. A., Mishonov, A. V., Baranova, O. K., Boyer, T. P., Zweng, Garcia, H. E., Reagan, J. R., Ainley, D., Weathers, K. W., Paver, C. R. and Smolyar, I. V. (2019). World Ocean Atlas 2018, *NOAA Atlas NESDIS 81* **1: Temperature**: 52.

Lorenz, D. J. and Hartmann, D. L. (2003). Eddy–Zonal Flow Feedback in the Northern Hemisphere Winter, *Journal of Climate* **16**: 16.

Lu, S., Lin, G., Liu, H., Ye, C., Que, H. and Ding, Y. (2019). A Weekly Load Data Mining Approach Based on Hidden Markov Model, *IEEE Access* **7**: 34609–34619.

Lukas, R. and Lindstrom, E. (1991). The mixed layer of the western equatorial Pacific Ocean, *Journal of Geophysical Research* **96**(S01): 3343.

Luo, D., Gong, T. and Diao, Y. (2007). Dynamics of Eddy-Driven Low-Frequency Dipole Modes. Part III: Meridional Displacement of Westerly Jet Anomalies during Two Phases of NAO, *Journal of the Atmospheric Sciences* **64**(9): 3232–3248.

MacLachlan, C., Arribas, A., Peterson, K. A., Maidens, A., Fereday, D., Scaife, A. A., Gordon, M., Vellinga, M., Williams, A., Comer, R. E., Camp, J., Xavier, P. and Madec, G. (2015). Global Seasonal forecast system version 5 (GloSea5): a high-resolution seasonal forecast system: GloSea5: A High-Resolution Seasonal Forecast System, *Quarterly Journal of the Royal Meteorological Society* **141**(689): 1072–1084.

Marcello, J., Hernández-Guerra, A., Eugenio, F. and Fonte, A. (2011). Seasonal and temporal study of the northwest African upwelling system, *International Journal of Remote Sensing* **32**(7): 1843–1859.

Martínez-Asensio, A., Marcos, M., Tsimplis, M. N., Gomis, D., Josey, S. and Jordà, G. (2014). Impact of the atmospheric climate modes on Mediterranean sea level variability, *Global and Planetary Change* **118**: 1–15.

Martínez-Asensio, A., Tsimplis, M. N., Marcos, M., Feng, X., Gomis, D., Jordà, G. and Josey, S. A. (2016). Response of the North Atlantic wave climate to atmospheric modes of variability: RESPONSE WAVE CLIMATE ATMOSPHERIC MODES, *International Journal of Climatology* **36**(3): 1210–1225.

Mawren, D. and Reason, C. J. C. (2017). Variability of upper-ocean characteristics and tropical cyclones in the South West Indian Ocean, *Journal of Geophysical Research: Oceans* **122**: 2012–2028.

McDougall, T. J. and Barker, P. M. (2011). *Getting started with TEOS-10 and the Gibbs Seawater (GSW) Oceanographic Toolbox*, Vol. 3.06.3 of *SCOR/IAPSO WG127*.
URL: *www.TEOS-10.org*

McGregor, H. V., Dima, M., Fischer, H. W. and Mulitza, S. (2007). Rapid 20th-Century Increase in Coastal Upwelling off Northwest Africa, *Science* **315**: 637–639.

Menge, B. A. and Menge, D. N. L. (2013). Dynamics of coastal meta-ecosystems: the intermittent upwelling hypothesis and a test in rocky intertidal regions, *Ecological Monographs* **83**(3): 283–310.

Messié, M. and Chavez, F. P. (2015). Seasonal regulation of primary production in eastern boundary upwelling systems, *Progress in Oceanography* **134**: 1–18.

Miller, J. A. and Shanks, A. L. (2004). Ocean-estuary coupling in the Oregon upwelling region: abundance and transport of juvenile fish and of crab megalopae, *Marine Ecology Progress Series* **271**: 267–279.

Moon, J.-H. and Song, Y. T. (2014). Seasonal salinity stratifications in the near-surface layer from Aquarius, Argo, and an ocean model: Focusing on the tropical Atlantic/Indian Oceans, *Journal of Geophysical Research: Oceans* **119**(9): 6066–6077.

Moore, G. W. K., Renfrew, I. A. and Pickart, R. S. (2013). Multidecadal Mobility of the North Atlantic Oscillation, *Journal of Climate* **26**(8): 2453–2466.

Narayan, N., Paul, A., Mulitza, S. and Schulz, M. (2010). Trends in coastal upwelling intensity during the late 20th century, *Ocean Science* **6**(3): 815–823.

Neves, M. C., Jerez, S. and Trigo, R. M. (2019). The response of piezometric levels in Portugal to NAO, EA, and SCAND climate patterns, *Journal of Hydrology* **568**: 1105–1117.

NOAA (2019). World Ocean Atlas 2018 (WOA18, National Oceanic and Atmospheric Administration).
URL: *https://www.nodc.noaa.gov/OC5/woa18/*

NOAA (2020a). East Atlantic (EA).
URL: *https://www.cpc.ncep.noaa.gov/data/teledoc/ea.shtml*

NOAA (2020b). North Atlantic Oscillation (NAO).
URL: *https://www.cpc.ncep.noaa.gov/products/precip/CWlink/pna/nao.shtml*

NOAA ERDDAP (2019). FNMOC Wind and Ekman Transport Data, 360x180, Monthly, from 6-hr Pressure.
URL: *https://coastwatch.pfeg.noaa.gov/erddap/*

NOAA Fisheries (2019). Upwelling Indices.
URL: *https://oceanview.pfeg.noaa.gov/products/upwelling/bakun*

Norton, J. G., Schwing, F. B., Pickett, M. H., Cummings, S. G., Husby, D. M. and Jessen, P. G. (2002). Monthly Mean Coastal Upwelling Indices, West Coast of South Africa 1981 to 2000: Trends and Relationships, p. 44.

Nykjær, L. and Van Camp, L. (1994). Seasonal and interannual variability of coastal upwelling along northwest Africa and Portugal from 1981 to 1991, *Journal of Geophysical Research* **99**(C7): 14,197–14,207.

Obata, A., Ishizaka, J. and Endoh, M. (1996). Global verification of critical depth theory for phytoplankton bloom with climatological in situ temperature and satellite ocean color data, *Journal of Geophysical Research: Oceans* **101**(C9): 20657–20667.

Pailler, K., Bourlès, B. and Gouriou, Y. (1999). The barrier layer in the western tropical Atlantic Ocean, *Geophysical Research Letters* **26**(14): 2069–2072.

Pardo, P., Padín, X., Gilcoto, M., Farina-Busto, L. and Pérez, F. (2011). Evolution of upwelling systems coupled to the long-term variability in sea surface temperature and Ekman transport, *Climate Research* **48**(2): 231–246.

Pearson, K. (1895). Notes on Regression and Inheritance in the Case of Two Parents, *Proceedings of the Royal Society of London* **58**: 240–242.

Pelegrí, J. L. and Benazzouz, A. (2015). Coastal Upwelling off North West Africa, *in* L. Valdés and I. Déniz-González (eds), *Oceanographic and biological features in the Canary Current Large Marine Ecosystem*, number 115 in *IOC Technical Series*, IOC-UNESCO, Paris, pp. 93–103.

Polo, I., Lazar, A., Rodriguez-Fonseca, B. and Arnault, S. (2008). Oceanic Kelvin waves and tropical Atlantic intraseasonal variability: 1. Kelvin wave characterization, *Journal of Geophysical Research* **113**(C7): C07009.

Polonsky, A. B. (1995). On the calculation of the depth of the upper mixed layer in the equatorial ocean, *Physical Oceanography* **6**(1): 51–59.

Polonsky, A. B. and Serebrennikov, A. N. (2018). Long-Term Sea Surface Temperature Trends in the Canary Upwelling Zone and their Causes, *Izvestiya, Atmospheric and Oceanic Physics* **54**(9): 1062–1067.

Ramos, A. M., Pires, A. C., Sousa, P. M. and Trigo, R. M. (2013). The use of circulation weather types to predict upwelling activity along the western Iberian Peninsula coast, *Continental Shelf Research* **69**: 38–51.

Rodgers, J. L. and Nicewander, W. A. (1988). Thirteen Ways to Look at the Correlation Coefficient, *The American Statistican* **42**(1): 59–66.

Rodwell, M. J., Rowell, D. P. and Folland, C. K. (1999). Oceanic forcing of the wintertime North Atlantic Oscillation and European climate, *Nature* **398**(6725): 320–323.

Roy, C. and Reason, C. (2001). ENSO related modulation of coastal upwelling in the eastern Atlantic, *Progress in Oceanography* **49**(1-4): 245–255.

Ryther, J. H. (1969). Photosynthesis and Fish Production in the Sea, *Science, New Series* **166**(3901): 72–76.

Santos, A. M. P., Kazmin, A. S. and Peliz, l. (2005). Decadal changes in the Canary upwelling system as revealed by satellite observations: Their impact on productivity, *Journal of Marine Research* **63**(2): 359–379.

Santos, F., Gómez-Gesteira, M., Decastro, M. and Álvarez, I. (2011). Upwelling along the western coast of the Iberian Peninsula: dependence of trends on fitting strategy, *Climate Research* **48**(2): 213–218.

Schlesinger, M. E. and Ramankutty, N. (1994). An oscillation in the global climate system of period 65-70 years, *Nature* **367**(6465): 723–726.

Serreze, M. C., Carse, F., Barry, R. G. and Rogers, J. C. (1997). Icelandic Low Cyclone Activity: Climatological Features, Linkages with the NAO, and Relationships with Recent Changes in the Northern Hemisphere Circulation, *Journal of Climate* **10**: 12.

Somavilla, R., González-Pola, C. and Fernández-Diaz, J. (2017). The warmer the ocean surface, the shallower the mixed layer. How much of this is true?, *Journal of Geophysical Research: Oceans* **122**(9): 7698–7716.

Sprintall, J. and Tomczak, M. (1992). Evidence of the barrier layer in the surface layer of the tropics, *Journal of Geophysical Research* **97**(C5): 7305.

Storto, A., Masina, S. and Navarra, A. (2016). Evaluation of the CMCC eddy-permitting global ocean physical reanalysis system (C-GLORS, 1982-2012) and its assimilation components: Evaluation of C-GLORS Global Ocean Reanalysis, *Quarterly Journal of the Royal Meteorological Society* **142**(695): 738–758.

Sverdrup, H. U. (1953). On Conditions for the Vernal Blooming of Phytoplankton, *ICES Journal of Marine Science* **18**(3): 287–295.

Sydeman, W. J., García-Reyes, M., Schoeman, D. S., Rykaczewski, R. R., Thompson, S. A., Black, B. A. and Bograd, S. J. (2014). Climate change and wind intensification in coastal upwelling ecosystems, *Science* **345**(6192): 77–80.

Tamim, A., Minaoui, K., Daoudi, K., Yahia, H., Atillah, A., El Fellah, S., Aboutajdine, D. and El Ansari, M. (2019). Automatic detection of Moroccan coastal upwelling zones using sea surface temperature images, *International Journal of Remote Sensing* **40**(7): 2648–2666.

Tanguy, Y., Arnault, S. and Lattes, P. (2010). Isothermal, mixed, and barrier layers in the subtropical and tropical Atlantic Ocean during the ARAMIS experiment, *Deep Sea Research Part I: Oceanographic Research Papers* **57**(4): 501–517.

Trigo, R. M., Pozo-Vázquez, D., Osborn, T. J., Castro-Díez, Y., Gámiz-Fortis, S. and Esteban-Parra, M. J. (2004). North Atlantic oscillation influence on precipitation, river flow and water resources in the Iberian Peninsula, *International Journal of Climatology* **24**(8): 925–944.

Troupin, C., Sangrà, P. and Arístegui, J. (2010). Seasonal variability of the oceanic upper layer and its modulation of biological cycles in the Canary Island region, *Journal of Marine Systems* **80**(3-4): 172–183.

Visbeck, M., Chassignet, E. P., Curry, R. G., Delworth, T. L., Dickson, R. R. and Krahmann, G. (2003). The ocean's response to North Atlantic Oscillation variability, *in* J. W. Hurell, Y. Kushnir and M. Visbeck (eds), *The North Atlantic Oscillation: Climatic significance and environmental impact*, American Geophysical Union, Washington, D. C., pp. 113–145.

Wang, J., Yang, B., Ljungqvist, F. C., Luterbacher, J., Osborn, T., Briffa, K. R. and Zorita, E. (2017). Internal and external forcing of multidecadal Atlantic climate variability over the past 1,200 years, *Nature Geoscience* **10**(7): 512–517.

Whitney, F. A. and Freeland, H. J. (1999). Variability in upper-ocean water properties in the NE Pacific Ocean, *Deep Sea Research Part II* **46**: 2351–2370.

Willis, J. K. (2004). Interannual variability in upper ocean heat content, temperature, and thermosteric expansion on global scales, *Journal of Geophysical Research* **109**(C12): C12036 (1–13).

Wooster, W. S., Bakun, A. and McLain, D. R. (1976). The seasonal upwelling cycle along the eastern boundary of the North Atlantic, *Journal of Marine Research* **34**(2): 131–141.

Wright, J., Brown, E., Colling, A., Par, D., Phillips, J. and Rothery, D. (2001). Coastal Upwelling in Eastern Boundary Currents, *in* G. Bearman (ed.), *Ocean Circulation*, Open University, Milton Keynes, pp. 133–137.

Yamaguchi, R. and Suga, T. (2019). Trend and Variability in Global Upper-Ocean Stratification Since the 1960s, *Journal of Geophysical Research: Oceans* **124**(12): 8933–8948.

Yamamoto, A., Tatebe, H. and Nonaka, M. (2020). On the Emergence of the Atlantic Multidecadal SST Signal: A Key Role of the Mixed Layer Depth Variability Driven by North Atlantic Oscillation, *Journal of Climate* **33**(9): 3511–3531.

Yan, Z., Tsimplis, M. N. and Woolf, D. (2004). Analysis of the relationship between the North Atlantic oscillation and sea-level changes in northwest Europe, *International Journal of Climatology* **24**(6): 743–758.

Yu, L. and Weller, R. A. (2007). Objectively Analyzed Air–Sea Heat Fluxes for the Global Ice-Free Oceans (1981–2005), *Bulletin of the American Meteorological Society* **88**(4): 527–540.

Zuo, H., Balmaseda, M. A., de Boisseson, E., Hirahara, S., Chrust, M. and de Rosnay, P. (2017). A new ensemble generation scheme for data assimilation and ocean analysis, *ECMWF Technical Memoranda* (795).

Zweng, M., Reagan, J. R., Seidov, D., Boyer, T. P., Locarnini, R. A., Garcia, H. E., Mishonov, A. V., Baranova, O. K., Weathers, K. W., Paver, C. R. and Smolyar, I. V. (2019). World Ocean Atlas 2018, *NOAA Atlas NESDIS 82* **Volume 2: Salinity**: 50.

IV Annex

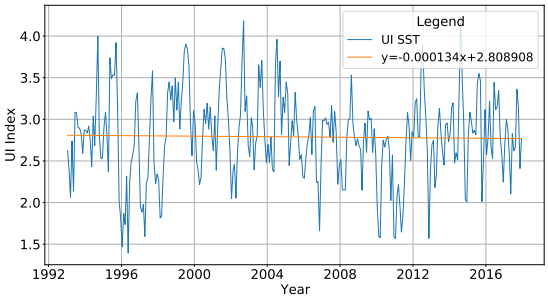

(a) UI_{SST}: 25.5°N

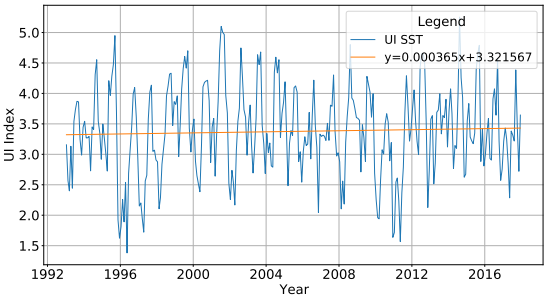

(b) UI_{SST}: 26.5°N

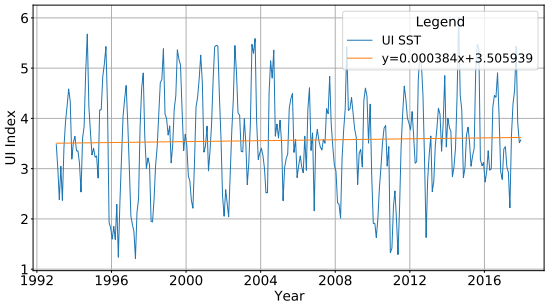

(c) UI_{SST}: 27.5°N

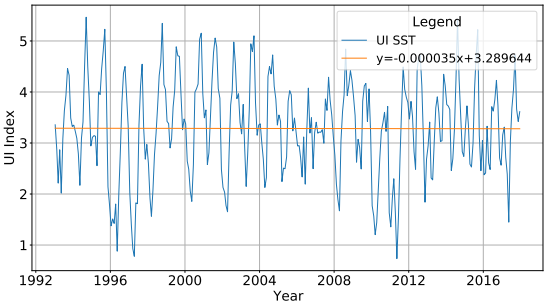

(d) UI_{SST}: 28.5°N

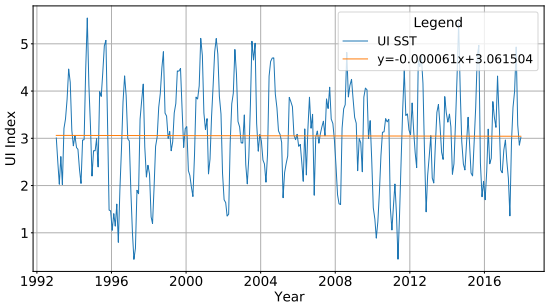

(e) UI_{SST}: 29.5°N

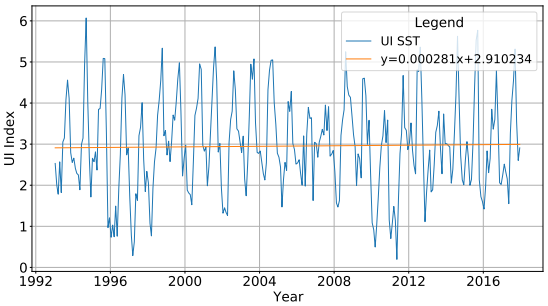

(f) UI_{SST}: 30.5°N

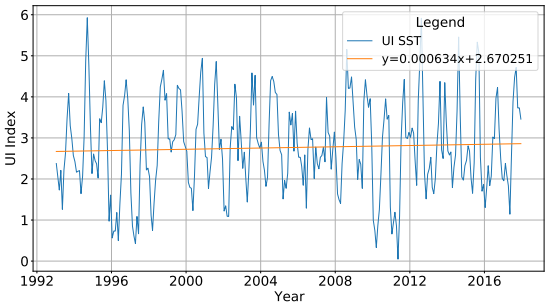

(g) UI_{SST}: 31.5°N

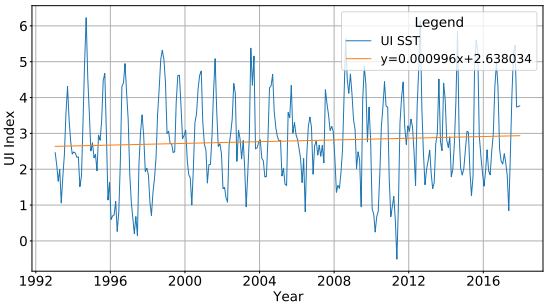

(h) UI_{SST}: 32.5°N

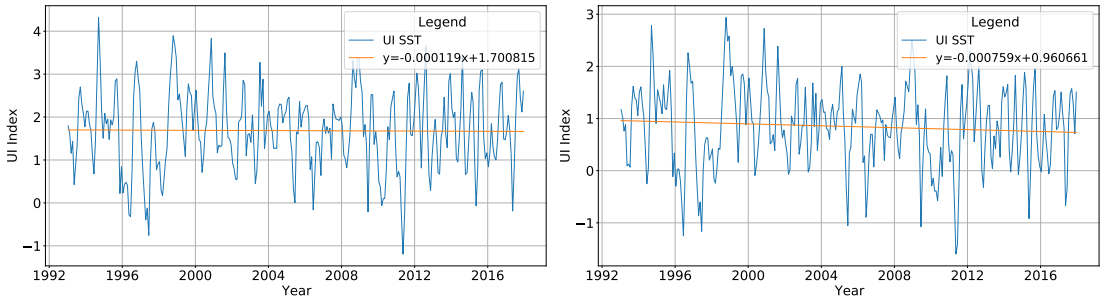

(i) UI_{SST}: 33.5°N **(j)** UI_{SST}: 34.5°N

Figure A.1: UI_{SST}: Time series per latitude. Time series (blue) and trendline (orange), trend calculated using linear regression (function see legend, plots created in Python using data obtained from: E.U. Copernicus Marine Service Information 2020, GREP, PHY_001_026).

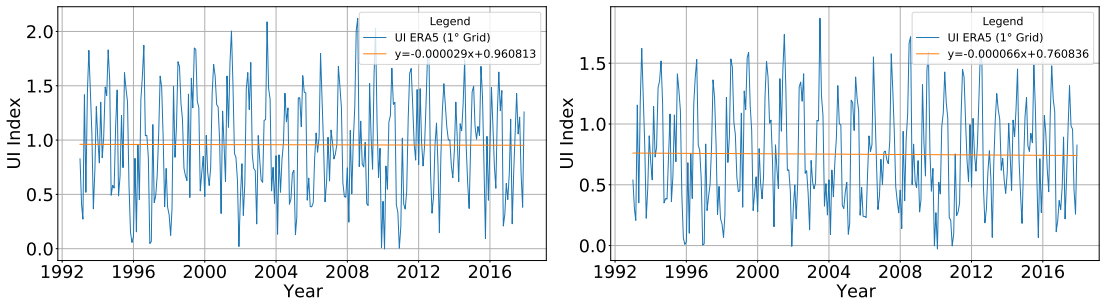

(a) UI_{ERA5}: 25.5°N **(b)** UI_{ERA5}: 26.5°N

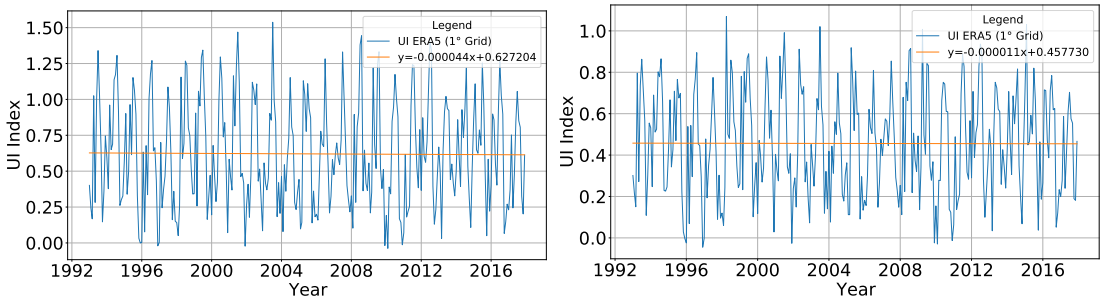

(c) UI_{ERA5}: 27.5°N **(d)** UI_{ERA5}: 28.5°N

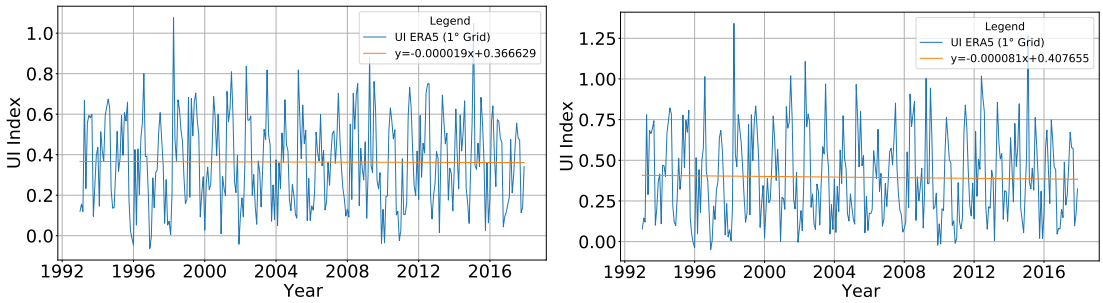

(e) UI_{ERA5}: 29.5°N **(f)** UI_{ERA5}: 30.5°N

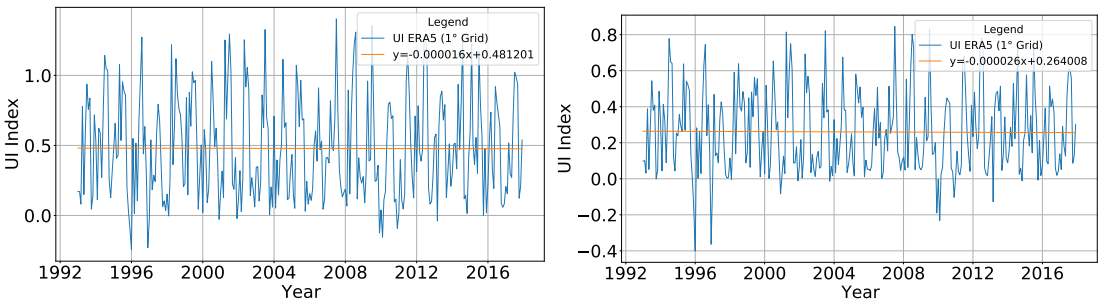

(g) UI_{ERA5}: 31.5°N

(h) UI_{ERA5}: 32.5°N

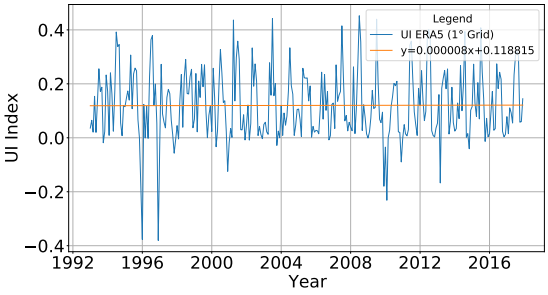

(i) UI_{ERA5}: 33.5°N

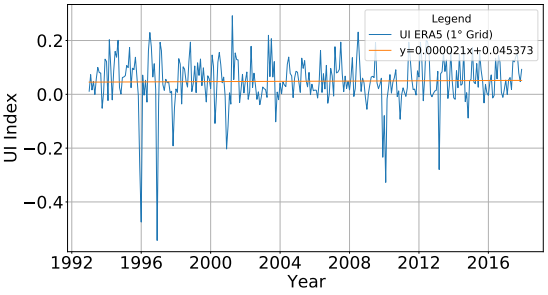

(j) UI_{ERA5}: 34.5°N

Figure A.2: UI_{ERA5}: Time series per latitude. Time series (blue) and trendline (orange), trend calculated using linear regression (function see legend, plots created in Python using data obtained by ECMWF: ECMWF Copernicus 2019).

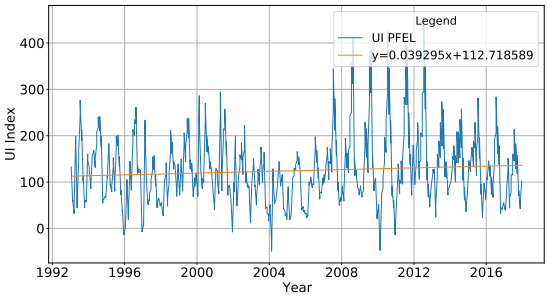

(a) UI_{PFEL}: 25.5°N

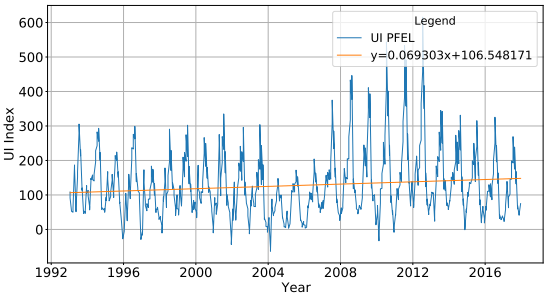

(b) UI_{PFEL}: 26.5°N

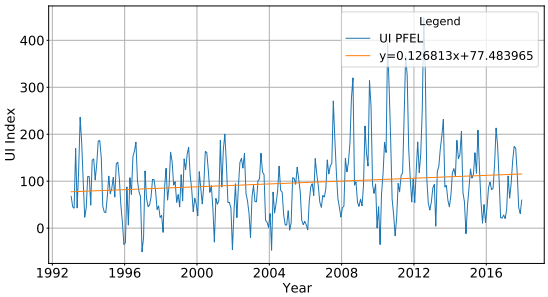

(c) UI_{PFEL}: 27.5°N

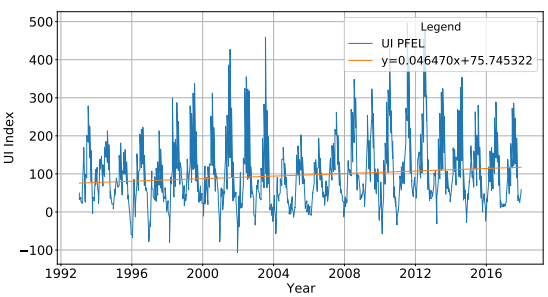

(d) UI_{PFEL}: 28.5°N

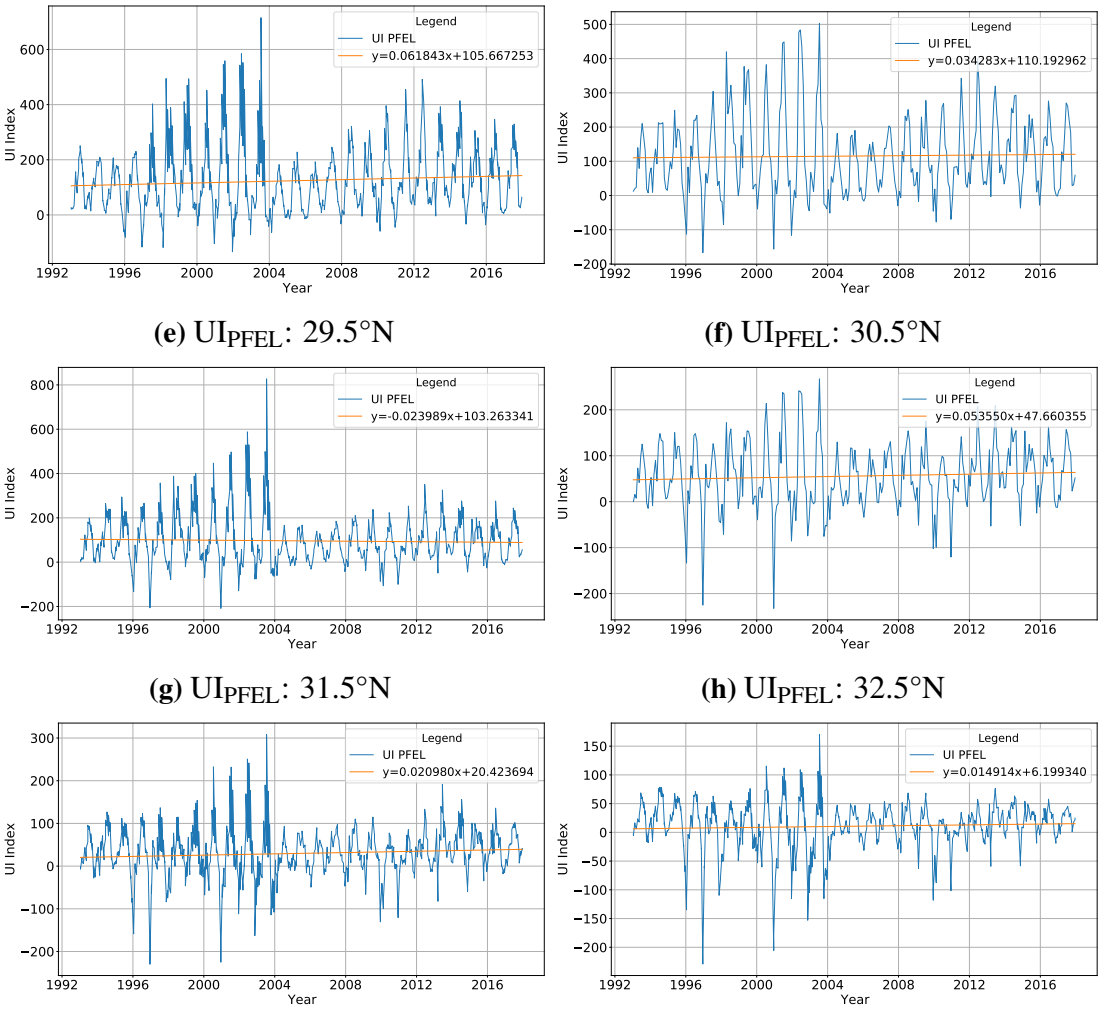

(e) UI_{PFEL}: 29.5°N **(f)** UI_{PFEL}: 30.5°N

(g) UI_{PFEL}: 31.5°N **(h)** UI_{PFEL}: 32.5°N

(i) UI_{PFEL}: 33.5°N **(j)** UI_{PFEL}: 34.5°N

Figure A.3: UI_{PFEL}: Time series per latitude. Time series (blue) and trendline (orange), trend calculated using linear regression (function see legend, plots created in Python using data obtained by PFEL: NOAA Fisheries 2019).

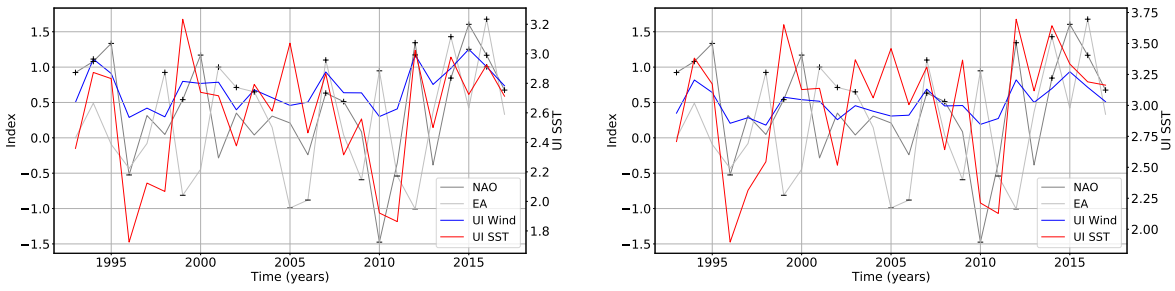

(a) 25.5°N **(b)** 26.5°N

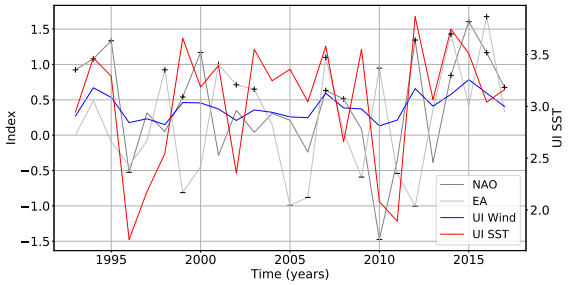

(c) 27.5°N

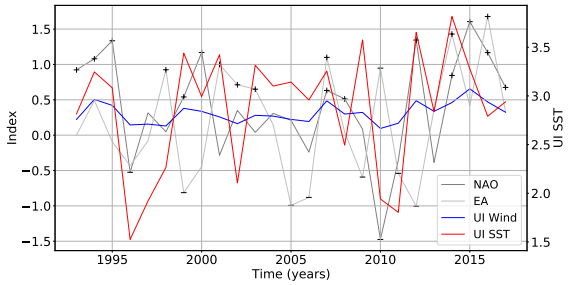

(d) 28.5°N

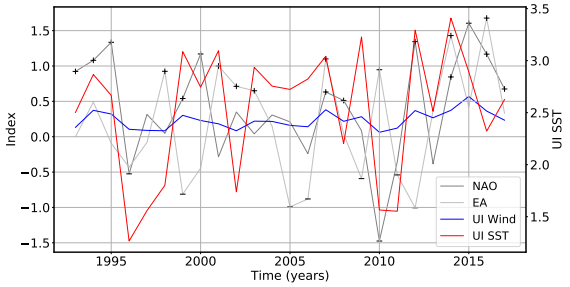

(e) 29.5°N

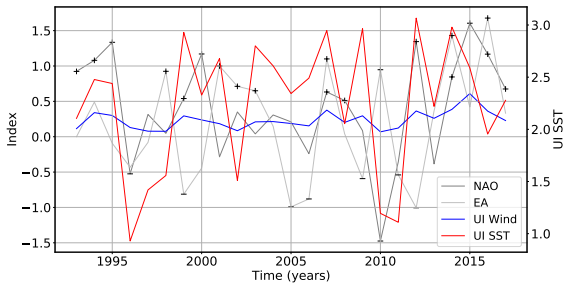

(f) 30.5°N

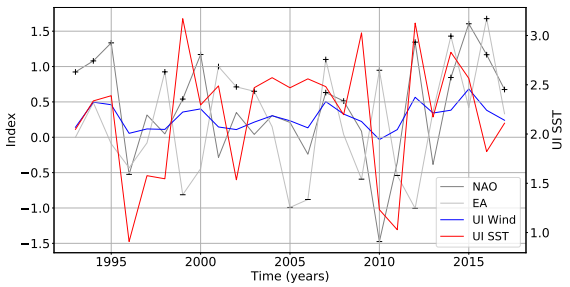

(g) 31.5°N

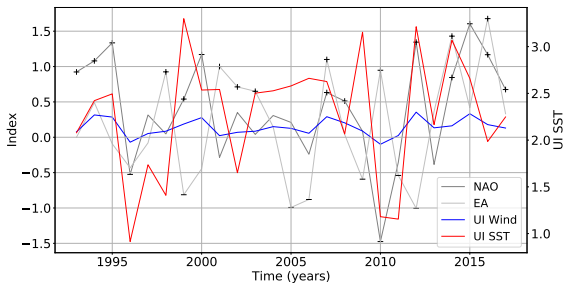

(h) 32.5°N

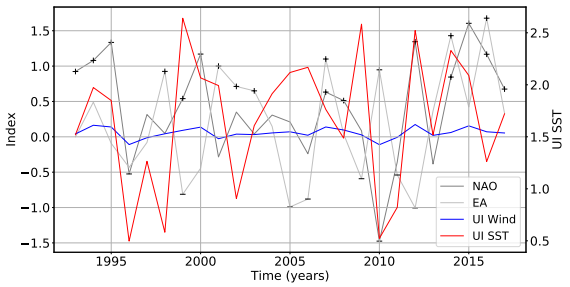

(i) 33.5°N

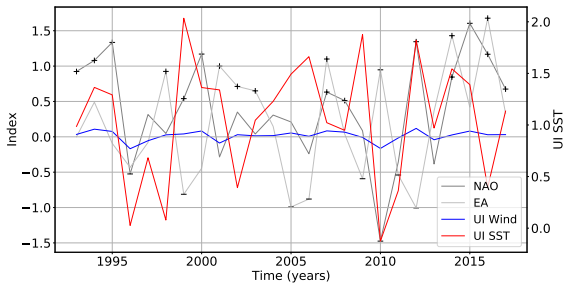

(j) 34.5°N

Figure A.4: Time Series of the Climate Pattern and the UI's per Latitude. Winter means of the NAO, EA (gray) and UI_{SST} and UI_{ERA5} for each latitude. Available positive events of the Climate Pattern (>0.5) and the UI_{ERA5} (>1.5) marked with '+', negative events (<-0.5, <-0.4) with '-' (threshold criterion of -1 and 5°C for the UI_{SST} not met, plots created in Python, data obtained from E.U. Copernicus Marine Service Information 2020, and ECMWF Copernicus 2019).

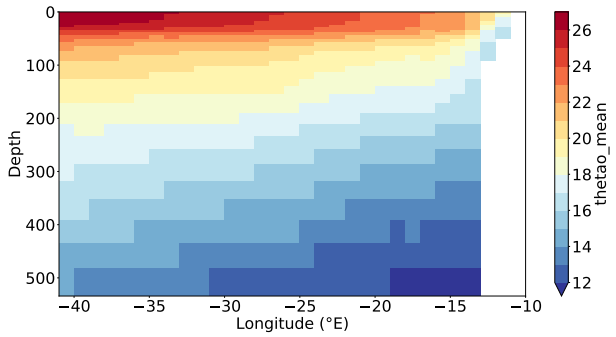

Figure A.5: UI_{SST}: Vertical composite map at 28.5°N. Plot showing the variation of the upper ocean structure along the longitudes (plots created in Python, data obtained from E.U. Copernicus Marine Service Information 2020).

Latitude (°N)	**Pearsons Correlation**		
	ILD-UI_{SST}	ILD-UI_{ERA5}	ILD-UI_{PFEL}
25.5	-0.182	-0.163	-0.148
26.5	-0.319	-0.212	-0.237
27.5	-0.354	-0.289	-0.318
28.5	-0.293	-0.127	-0.269
29.5	-0.343	-0.155	-0.341
30.5	-0.440	-0.144	-0.312
31.5	-0.399	-0.264	-0.369
32.5	-0.264	-0.182	-0.306
33.5	-0.049	-0.280	-0.381
34.5	0.223	-0.119	-0.377

Table A.1: Pearsons correlation coefficient between the ILD and the UI's. Correlation of the coastal ILD and UI for each latitude of the study area (correlation values rounded).

Year	**Climate Pattern**		**Month**						
	NAO	EA	5	6	7	8	9	10	11
1993	0.92	0.00							
1994	1.08	0.49					6.23 (32.5)		
1995	1.33	-0.09				5.09 (30.5)	5.43 (27.5)		
1996	-0.53	-0.43		-1.25 (34.5)					
1997	0.32	-0.08		-1.16 (34.5)					
1998	0.05	0.93					5.07 (32.5)	5.39 (27.5)	5.06 (32.5)

Tab. A.2, to be continued.

Continued tab. A.2									
Year	**Climate Pattern**		**Month**						
	NAO	EA	5	6	7	8	9	10	11
1999	0.54	-0.81			5.36 (27.5)	5.18 (27.5)	5.06 (27.5)		
2000	1.17	-0.45						5.26 (27.5)	5.15 (28.5)
2001	-0.29	1.00			5.42 (27.5)	5.45 (27.5)	5.44 (27.5)		
2002	0.35	0.71				5.45 (27.5)			
2003	0.04	0.65			5.47 (27.5)	5.3 (27.5)	5.59 (27.5)		
2004	0.31	0.15			5.15 (27.5)	5.04 (30.5)	5.36 (27.5)		
2005	0.21	-0.99		-1.05 (34.5)					
2006	-0.24	-0.88							
2007	0.63	1.10							
2008	0.51	0.04				5.64 (32.5)			
2009	0.09	-0.59		-1.08 (34.5)					
2010	-1.48	0.95							
2011	-0.36	-0.54	-1.6 (34.5)	-1.41 (34.5)					
2012	1.35	-1.01			5.26 (27.5)	6.13 (32.5)			
2013	-0.39	0.37							
2014	0.85	1.43				6.01 (27.5)			
2015	1.61	0.42				5.6 (32.5)	5.77 (30.5)		
2016	1.17	1.68							
2017	0.68	0.33				5.21 (32.5)	5.46 (32.5)		

Table A.2: Phases of the NAO and the EA with up- and downwelling events per year (UI_{SST}). Red text colors mark positive, blue negative phases of Climate Pattern, strength of the highest upwelling and downwelling values and the latitude marked in each month of their occurrence (summary of all latitudes).